The R-process Alliance: The Peculiar Chemical Abundance Pattern of RAVE J183013.5-455510

The Astrophysical Journal, 897:78 (21pp), 2020 July 1 https://doi.org/10.3847/1538-4357/ab99c6

The *R*-process Alliance: The Peculiar Chemical Abundance Pattern of RAVE J183013.5−455510*

Vinicius M. Placco[1,2], Rafael M. Santucci[3,4], Zhen Yuan[5], Mohammad K. Mardini[6,7], Erika M. Holmbeck[1,2], Xilu Wang[1,2,8], Rebecca Surman[1,2], Terese T. Hansen[9], Ian U. Roederer[2,10], Timothy C. Beers[1,2], Arthur Choplin[11,12], Alexander P. Ji[13,17], Rana Ezzeddine[14], Anna Frebel[2,15], Charli M. Sakari[16], Devin D. Whitten[1,2], and Joseph Zepeda[1,2]

[1] Department of Physics, University of Notre Dame, Notre Dame, IN 46556, USA; vplacco@nd.edu
[2] JINA Center for the Evolution of the Elements, USA
[3] Instituto de Estudos Sócio-Ambientais, Planetário, Universidade Federal de Goiás, Goiânia, GO 74055-140, Brazil
[4] Instituto de Física, Universidade Federal de Goiás, Campus Samambaia, Goiânia, GO 74001-970, Brazil
[5] Key Laboratory for Research in Galaxies and Cosmology, Shanghai Astronomical Observatory, Chinese Academy of Sciences, Shanghai 200030, People's Republic of China
[6] Key Laboratory of Optical Astronomy, National Astronomical Observatories, Chinese Academy of Sciences, Beijing, People's Republic of China
[7] School of Astronomy and Space Science, University of Chinese Academy of Sciences, Beijing, People's Republic of China
[8] Department of Physics, University of California, Berkeley, CA 94720, USA
[9] Mitchell Institute for Fundamental Physics and Astronomy and Department of Physics and Astronomy, Texas A & M University, College Station, TX 77843, USA
[10] Department of Astronomy, University of Michigan, Ann Arbor, MI 48109, USA
[11] Department of Physics, Faculty of Science and Engineering, Konan University, 8-9-1 Okamoto, Kobe, Hyogo 658-8501, Japan
[12] Geneva Observatory, University of Geneva, Maillettes 51, CH-1290 Sauverny, Switzerland
[13] Observatories of the Carnegie Institution for Science, Pasadena, CA 91101, USA
[14] Department of Astronomy, University of Florida, Bryant Space Science Center, Gainesville, FL 32611, USA
[15] Department of Physics and Kavli Institute for Astrophysics and Space Research, Massachusetts Institute of Technology, Cambridge, MA 02139, USA
[16] Department of Physics & Astronomy, San Francisco State University, San Francisco, CA 94132, USA
Received 2020 February 28; revised 2020 May 21; accepted 2020 June 1; published 2020 July 6

Abstract

We report on the spectroscopic analysis of RAVE J183013.5−455510, an extremely metal-poor star, highly enhanced in CNO, and with discernible contributions from the rapid neutron-capture process. There is no evidence of binarity for this object. At [Fe/H] = −3.57, this star has one of the lowest metallicities currently observed, with 18 measured abundances of neutron-capture elements. The presence of Ba, La, and Ce abundances above the solar system *r*-process predictions suggests that there must have been a non-standard source of *r*-process elements operating at such low metallicities. One plausible explanation is that this enhancement originates from material ejected at unusually high velocities in a neutron star merger event. We also explore the possibility that the neutron-capture elements were produced during the evolution and explosion of a rotating massive star. In addition, based on comparisons with yields from zero-metallicity faint supernova, we speculate that RAVE J1830−4555 was formed from a gas cloud pre-enriched by both progenitor types. From analysis based on Gaia DR2 measurements, we show that this star has orbital properties similar to the Galactic metal-weak thick-disk stellar population.

Unified Astronomy Thesaurus concepts: Chemical abundances (224); Stellar atmospheres (1584); Stellar kinematics (1608); R-process (1324); CEMP stars (2105); Metallicity (1031)

Supporting material: machine-readable table, interactive figure

1. Introduction

One of the most intriguing challenges in stellar astrophysics today is to paint a compelling picture of how the universe evolved chemically from hydrogen and helium (with traces of lithium) to the vast diversity of elements we observe today in the atmosphere of the Sun and other stars. Nucleosynthesis taking place during the evolution of stars, in either burning or explosive stages, is the culprit for such diversity (Merrill 1952; Hoyle 1954; Arnett 1996). The underlying physical processes by which chemical elements, from carbon to uranium, are formed has a reasonably well-established framework (e.g., Burbidge et al. 1957; Cameron 1957). The next steps are to identify possible astrophysical sites where such nucleosynthesis events could occur and describe the mixing processes that seed the formation of subsequent stellar generations.

Therefore, a star such as the Sun (with a main-sequence age of over 4 Gyr) was formed from a gas cloud that carried over 9 Gyr of chemical evolution from previous stellar generations. As a result of this, and the intrinsic stochasticity associated with star formation, it is impossible to pinpoint a single genealogical record for such relatively young stars. However, by observing stars formed from gas clouds enriched by a single (or a handful of) nucleosynthesis episode(s), as is expected to be the case for the most metal-deficient stars in the Galaxy, it is possible to characterize and study the progenitor population(s) of these stars.

The field of stellar archeology was built upon the premise that old, slowly evolving, low-mass, low-metallicity stars can preserve in their atmospheres the chemical imprint of primordial stellar populations in the Galaxy and the universe (Bromm & Larson 2004; Bromm et al. 2009; Nomoto et al. 2013). More importantly, it is believed that a subset of these

* Based on observations gathered with the 6.5 m Magellan Telescopes located at Las Campanas Observatory, Chile. Based on observations collected at the European Organisation for Astronomical Research in the Southern Hemisphere under ESO program 099.D-0428(A).
[17] Hubble Fellow.

objects are indeed "true" second-generation stars, also known as extremely metal-poor (EMP; [Fe/H][18] < -3.0) stars (Beers & Christlieb 2005). The chemical abundance patterns of these EMP stars can place direct constraints on the nature of the first (Population III) stars to be formed in the universe (e.g., Christlieb et al. 2002; Frebel et al. 2006, 2015; Norris et al. 2007; Caffau et al. 2011, 2016; Ito et al. 2013; Hansen et al. 2014; Keller et al. 2014; Placco et al. 2014a, 2016b; Starkenburg et al. 2014, 2018; Meléndez et al. 2016; Roederer et al. 2016; Aguado et al. 2018; Ezzeddine et al. 2019; Mardini et al. 2019a, 2019b) and possible astrophysical site(s) for their occurrence, such as dwarf galaxies (Salvadori et al. 2015; Hansen et al. 2017; Longeard et al. 2018; Nagasawa et al. 2018; Marshall et al. 2019) and damped Lyα systems (Cooke et al. 2011; Cooke & Madau 2014; Welsh et al. 2020).

A large fraction of EMP stars exhibit enhancements in carbon (and similarly nitrogen and oxygen—43% according to Placco et al. 2014c) and are classified as carbon-enhanced metal-poor (CEMP; [C/Fe] $> +0.7$, Aoki et al. 2007). These objects are further classified by their paucity or enhancement in neutron-capture elements (CEMP-no and CEMP-$s/r/i$, respectively—Beers & Christlieb 2005; Frebel 2018) and have very distinct nucleosynthetic pathways and enrichment processes (Yoon et al. 2016; Frebel 2018).

The light-element (from C to Zn) abundance pattern found in EMP stars (mostly CEMP-no) is believed to be the result of the evolution of massive Population III stars in the early universe. Candidates for the CEMP-no progenitor population are (i) metal-free massive stars (Heger & Woosley 2010), (ii) mixing and fallback "faint supernovae" (Umeda & Nomoto 2005; Nomoto et al. 2006; Tominaga et al. 2014), and (iii) rapidly rotating massive stars with near-zero metallicity (*spinstars;* Meynet et al. 2010; Cescutti et al. 2013; Chiappini 2013; Cescutti & Chiappini 2014). A subset of these EMP stars, also known as "mono-enriched," are thought to be the direct descendants of the first stars (Hartwig et al. 2018). Placco et al. (2016b) provide a brief explanation of the main characteristics of these progenitor types and the possible metallicity regimes where their occurrence appears to have better agreement with observations.

For the heavy elements (from Ga to U), formed by the *slow*, *intermediate*, and *rapid* neutron-capture processes (*s*-, *i*-, and *r*-processes; Frebel 2018; Hansen et al. 2019; Prantzos et al. 2020), there are a number of possible astrophysical sites responsible for their production. The observed *s*-process abundances in CEMP-*s*, CEMP-r/s, and CEMP-*i* stars[19] are thought to be a result of the evolution of low- to intermediate-mass, low-metallicity stars on the asymptotic giant branch (AGB) (Herwig 2005; Hampel et al. 2016). The newly synthesized elements are then moved to the atmosphere of the less-evolved low-metallicity companion via mass transfer in a binary system (Starkenburg et al. 2014; Hansen et al. 2015, 2016a; Cseh et al. 2018).

The onset and operation of the *r*-process require high neutron fluxes and densities. Possible astrophysical sites that would sustain these conditions include (i) the aftermath of events such as mergers of neutron stars (Abbott et al. 2017; Drout et al. 2017; Shappee et al. 2017), (ii) supernova-triggering collapse of rapidly rotating massive stars (*collapsars*; Siegel et al. 2019), and (iii) common-envelope jet supernovae (Grichener & Soker 2019). Observational evidence suggests that these events could have occurred early in the history of the universe (Roederer et al. 2014a) in environments such as dwarf galaxies, which were recently found to harbor low-metallicity, *r*-process enhanced stars (Ishimaru et al. 2015; Vincenzo et al. 2015; Ji et al. 2016; Hansen et al. 2017; Roederer 2017; Roederer et al. 2018a). However, there is still no consensus in the literature as to which *r*-process nucleosynthesis channel (or combination of channels) can successfully reproduce observations and be incorporated in models of Galactic chemical evolution (Matteucci et al. 2014; Cescutti et al. 2015; Shen et al. 2015; van de Voort et al. 2015; Wehmeyer et al. 2015; Côté et al. 2019; Haynes & Kobayashi 2019; Holmbeck et al. 2019).

From an observational perspective, the *R*-Process Alliance (RPA) has been instrumental in the quest to increase the number of known *r*-process enhanced stars in the Galaxy. In its two years of existence, the RPA has already identified 26 new *r*-II ([Eu/Fe] $> +1.0$) and 146 new *r*-I ($+0.3 \leqslant$ [Eu/Fe] $\leqslant +1.0$) stars (Hansen et al. 2018; Sakari et al. 2018a; Ezzeddine et al. 2020), an increase of 87% and 130%, respectively, from all previous literature studies.[20] This ongoing effort has already provided in-depth analyses of a number of unique low-metallicity stars in the Galaxy (e.g., Cain et al. 2018; Gull et al. 2018; Holmbeck et al. 2018; Roederer et al. 2018b; Sakari et al. 2018b) and will continue to do so in its next stages.

In this work, we report on the identification and analysis of RAVE J183013.5−455510 (hereafter RAVE J1830−4555), a CNO-enhanced extremely metal-poor ([Fe/H] $= -3.57$) star exhibiting discernible *r*- and *s*-process patterns, with chemical abundances measured for 18 neutron-capture elements. This ancient star belongs to the metal-weak thick-disk (MWTD) population of the Milky Way galaxy, and radial-velocity measurements spanning more than eight years show no variations outside 1σ. This paper is outlined as follows: Section 2 describes the medium- and high-resolution spectroscopic observations. The determinations of stellar parameters and chemical abundances are presented, respectively, in Sections 3 and 4, including a comparison with data from the literature. Analyses of radial-velocity variations, chemical abundance pattern, and the kinematics of RAVE J1830−4555 are presented in Section 5. Our conclusions are provided in Section 6.

2. Observations

RAVE J1830−4555 is a relatively bright ($V = 12$) star in the Southern Hemisphere, in a region not heavily obscured by dust. Table 1 lists basic photometric and astrometric information for RAVE J1830−4555; the top row of Figure 1 shows the finding charts from the Digitized Sky Survey (DSS blue and red; Lasker et al. 1990) and from the Two Micron All Sky Survey (2MASS; Skrutskie et al. 2006). Below we describe the medium-resolution and high-resolution spectroscopic observations of RAVE J1830−4555.

[18] $[X/Y] = \log(N_X/N_Y)_\star - \log(N_X/N_Y)_\odot$, where N is the number density of atoms of elements X and Y in the star ($\star$) and the Sun ($\odot$).

[19] CEMP-*s*: [C/Fe] $> +0.7$, [Ba/Fe] $> +1.0$, [Ba/Eu] $> +0.5$, and [Ba/Pb] > -1.5; CEMP-r/s: [C/Fe] $> +0.7$, $0.0 <$ **[Ba/Eu] $< +0.5$, and $-1.0 <$ ***[Ba/Pb] < -0.5; CEMP-*i*: [C/Fe] $> +0.7$, $0.0 <$ **[La/Eu] $< +0.6$, and [Hf/Ir] $\sim +1.0$. See Table 1 in Frebel (2018) for further details.

[20] Holmbeck et al. (2020) proposes a new dividing line between the *r*-I and *r*-II classes at [Eu/Fe] $= +0.7$, which changes the numbers of *r*-I and *r*-II stars identified by the RPA to 121 and 51, respectively.

Table 1
Observational Data for RAVE J183013.5−455510

Quantity	Symbol	Value	Units	References
R.A.	α (J2000)	18:30:13.54	hh:mm:ss.ss	Simbad[a]
Decl.	δ (J2000)	−45:55:10.1	dd:mm:ss.s	Simbad[a]
Galactic longitude	ℓ	348.9	deg	Simbad[a]
Galactic latitude	b	−15.7	deg	Simbad[a]
Gaia DR2 source ID		6708532208165979392		Gaia Collaboration et al. (2018)
Parallax	ϖ	0.3214 ± 0.0429	mas	Lindegren et al. (2018)
Inverse parallax distance	$1/\varpi$	$3.11^{+0.48}_{-0.37}$	kpc	this work
Distance	D	$2.88^{+0.43}_{-0.33}$	kpc	Bailer-Jones et al. (2018)
Distance	D	$2.75^{+0.58}_{-0.40}$	kpc	Anders et al. (2019)
Proper motion (α)	PMRA	7.949 ± 0.084	mas yr^{-1}	Lindegren et al. (2018)
Proper motion (δ)	PMDec	−6.712 ± 0.081	mas yr^{-1}	Lindegren et al. (2018)
G magnitude	G	11.8125 ± 0.0002	mag	Gaia Collaboration et al. (2018)
G_{BP} magnitude	G_{BP}	12.2984 ± 0.0015	mag	Gaia Collaboration et al. (2018)
G_{RP} magnitude	G_{RP}	11.1767 ± 0.0009	mag	Gaia Collaboration et al. (2018)
B magnitude	B	12.915 ± 0.010	mag	Henden & Munari (2014)
V magnitude	V	12.059 ± 0.010	mag	Henden & Munari (2014)
J magnitude	J	10.393 ± 0.023	mag	Skrutskie et al. (2006)
H magnitude	H	9.852 ± 0.022	mag	Skrutskie et al. (2006)
K magnitude	K	9.744 ± 0.020	mag	Skrutskie et al. (2006)
Color excess	$E(B-V)$	0.0486	mag	Schlafly & Finkbeiner (2011)
Radial velocities	RV	61.3 ± 1.9	km s^{-1}	Gaia DR2 (four epochs)
		63.5 ± 1.6	km s^{-1}	RAVE DR5 (MJD: 55743.622)
		61.1 ± 1.0	km s^{-1}	du Pont (MJD: 57894.294)
		63.2 ± 0.5	km s^{-1}	Magellan (MJD: 57979.596)
		62.4 ± 1.0	km s^{-1}	du Pont (MJD: 58734.518)

Note.
[a] http://simbad.u-strasbg.fr/simbad/sim-id?Ident=RAVE+J183013.5-455510

2.1. Medium-resolution Spectroscopy

RAVE J1830−4555 was first selected as a metal-poor star candidate from the fifth data release of the Radial Velocity Experiment (RAVE DR5; Steinmetz et al. 2006; Kunder et al. 2017) and followed up with medium-resolution spectroscopy as part of the validation efforts described in Placco et al. (2018, 2019). Observations were carried out in semester 2017A with the 3.58 m ESO New Technology Telescope (NTT), using the EFOSC-2 spectrograph (Buzzoni et al. 1984). The instrument setup included Grism7 (600 grooves mm^{-1}) and a 1.″0 slit, yielding a wavelength coverage of 3500–5200 Å, resolving power of $R \sim 2000$ (1 × 1 binning), and signal-to-noise ratio of S/N ∼ 50 per pixel at 4000 Å. Calibration frames included FeAr exposures, quartz-lamp flatfields, and bias frames. All reduction and extraction tasks were performed using IRAF[21] packages. Figure 1 (middle panel) shows a portion of the NTT spectrum, indicating absorption features and regions of interest for stellar parameter determination and chemical abundance analysis.

2.2. High-resolution Spectroscopy

High-resolution spectroscopy for RAVE J1830−4555 was obtained on 2017 August 14 using the Magellan Inamori Kyocera Echelle (MIKE; Bernstein et al. 2003) spectrograph, mounted on the 6.5 m Magellan–Clay Telescope at Las Campanas Observatory. The observing setup included a 0.″7 slit with 2 × 2 on-chip binning, yielding a resolving power of $R \sim 37{,}000$ (blue spectrum) and $R \sim 30{,}000$ (red spectrum). The S/N is ∼80 per pixel at 3900 Å and ∼120 at 5200 Å after a total exposure of 2000 s. The MIKE spectrum covers a wide range of optical wavelengths (∼3300–9000 Å), making it ideal for chemical abundance determinations, in particular for neutron-capture elements (see Section 4 for details). The data were reduced using the routines developed for MIKE spectra, described in Kelson (2003).[22] The colored panels of Figure 1 show selected regions of the MIKE spectrum, highlighting atomic and molecular features of interest for abundance determination. RAVE J1830−4555 was also observed in the 2017A and 2019B semesters with the Echelle spectrograph on the du Pont 2.5 m telescope at the Las Campanas Observatory, as part of the RPA snapshot campaign (see Hansen et al. 2018, for further details). These spectra were used to confirm the atmospheric parameters determined for the MIKE spectrum and also for comparisons of radial velocity. The observational data and radial velocities for RAVE J1830−4555 are listed in Table 1.

3. Stellar Atmospheric Parameters

3.1. Medium-resolution Spectrum

Stellar atmospheric parameters (T_{eff}, log g, and [Fe/H]) were calculated from the ESO/NTT spectrum using the n-SSPP (Beers et al. 2014, 2017), a modified version of the SEGUE Stellar Parameter Pipeline (SSPP; Lee et al. 2008a, 2008b, 2013). These were used to flag RAVE J1830−4555 as a

[21] http://iraf.noao.edu

[22] http://code.obs.carnegiescience.edu/python

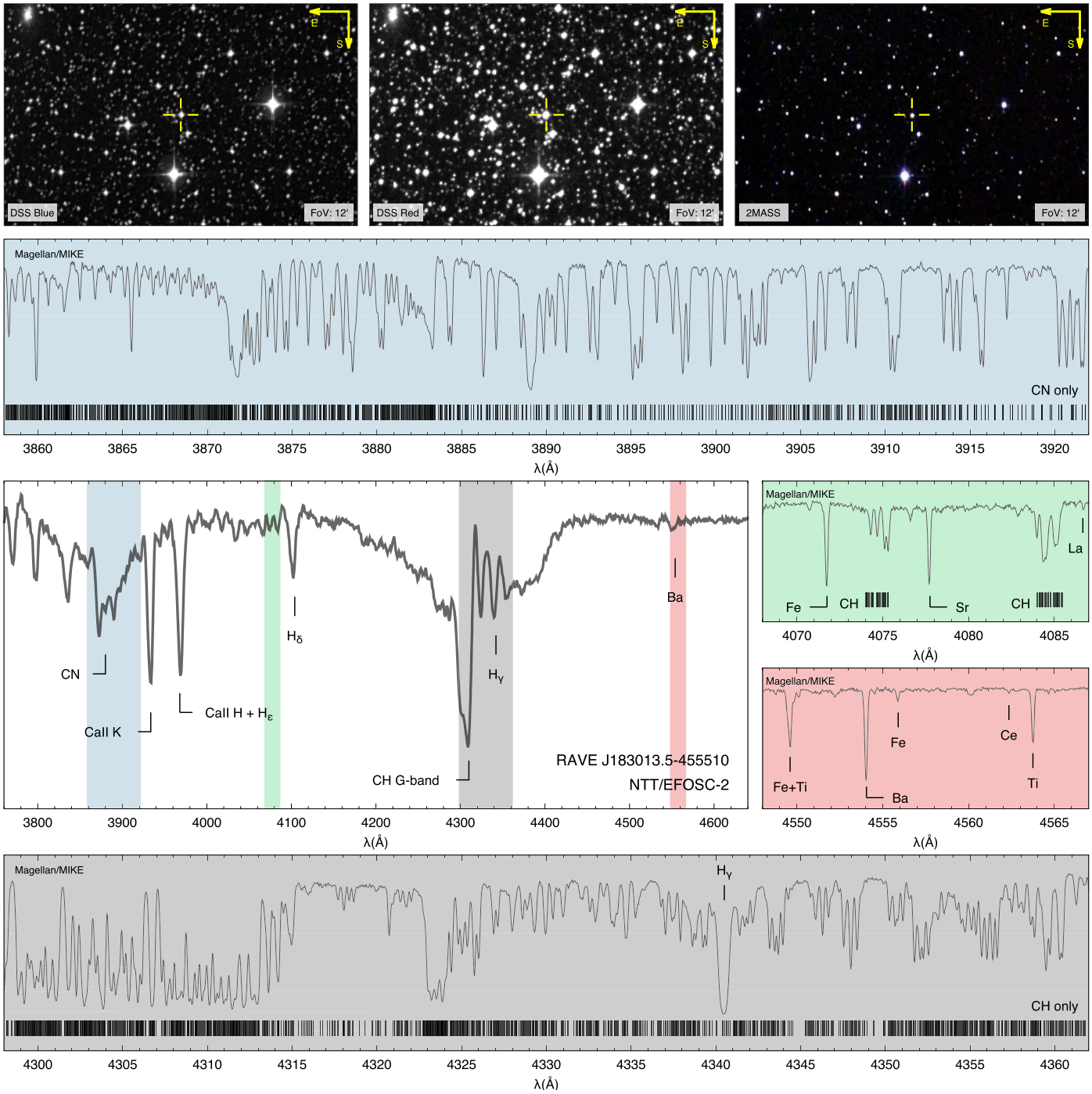

Figure 1. Top row: DSS (blue/red) and 2MASS (combined) finding charts for RAVE J1830−4555. Middle panel: medium-resolution NTT spectrum. Colored panels: selected regions of the high-resolution Magellan spectrum. Atomic and molecular features of interest used in the analysis are highlighted. An interactive version of this figure can be accessed at https://vmplacco.github.io/J1830-4555.html.

candidate for high-resolution spectroscopic follow-up. The parameters were also estimated by the CASPER (Chemical Abundance and Stellar Parameter Estimation Routine) software, described in Yoon et al. (2020). CASPER also estimated the carbon abundance for RAVE J1830−4555 as $\log \epsilon(\mathrm{C}) = +6.82 \pm 0.24$, which is in excellent agreement with the value determined from the high-resolution spectrum ($\log \epsilon(\mathrm{C}) = +6.76 \pm 0.10$; see Section 4.1 for further details). The final parameters are listed in Table 2, together with values from the literature and the high-resolution spectra (see details below).

3.2. High-resolution Spectra

The stellar parameters for the high-resolution data were determined spectroscopically, using the latest version of the MOOG[23] code (Sneden 1973), employing one-dimensional plane-parallel model atmospheres with no overshooting (Castelli & Kurucz 2003), and computed under the assumption of local thermodynamic equilibrium. The effective temperature

[23] https://github.com/alexji/moog17scat

Table 2
Derived Stellar Parameters

	$T_{\rm eff}$ (K)	log g (cgs)	[Fe/H]	ξ (km s^{-1})
Literature values				
Gaia	4993 (100)	⋯	⋯	⋯
RAVE	4984 (100)	3.34 (0.47)	−3.51 (0.16)	⋯
This work				
ESO/NTT	4781 (150)	0.95 (0.35)	−4.15 (0.20)	⋯
CASPER	4905 (150)	1.70 (0.40)	−3.84 (0.16)	⋯
du Pont	4720 (100)	1.40 (0.20)	−3.56 (0.10)	2.00 (0.20)
Magellan	4765 (100)	1.20 (0.20)	−3.57 (0.10)	1.95 (0.20)

was determined by minimizing the trend between the abundances of individual Fe I lines and their excitation potential (χ). After that, the temperature is corrected to the "photometric scale" using the calibration described in Frebel et al. (2013). With the temperature fixed, the microturbulent velocity (ξ) was determined by removing the trend in the Fe I abundances and the reduced equivalent width (REW = log(EW/λ)), and the surface gravity was determined by forcing the agreement between the Fe I and Fe II average abundances. The equivalent widths were obtained automatically by fitting Gaussian profiles to the observed absorption lines and then visually inspected. Table 3 lists the lines employed in this analysis, their measured equivalent widths, and the derived chemical abundances. This procedure was used to determine the parameters using both the du Pont/Echelle and Magellan/MIKE spectra. The resulting parameters are listed in Table 2.

4. Chemical Abundances

Elemental abundance ratios, [X/Fe], were calculated adopting the solar photospheric abundances from Asplund et al. (2009). The average measurements (or upper limits) for 36 elements, derived from the Magellan/MIKE spectrum, are listed in Table 4. The σ values are the standard error of the mean. Abundances were calculated by both equivalent-width analysis and spectral synthesis.

Uncertainties in the elemental abundance determinations, as well as the systematic uncertainties due to changes in the atmospheric parameters, were treated in the same way as described in Placco et al. (2013, 2015). Table 5 shows how variations within the quoted uncertainties in each atmospheric parameter affect the derived chemical abundances. Also listed is the total uncertainty for each element, which is calculated from the quadratic sum of the individual error estimates. For this purpose, we used spectral features with abundances determined by equivalent-width analysis only. The adopted variations for the parameters are +150 K for $T_{\rm eff}$, +0.3 dex for log g, and +0.3 km s^{-1} for ξ.

4.1. Carbon, Nitrogen, and Oxygen

The carbon abundance for RAVE J1830−4555 was derived from nine different regions of the MIKE spectrum, including CH/C_2 molecules and a C I atomic feature. All of the individual abundances (listed in Table 3) are within 0.12 dex; the average value found is $\log\epsilon$(C) = 6.76 ([C/Fe] = +1.90).

Table 3
Equivalent-width Measurements

Ion	λ (Å)	χ (eV)	log gf	EW (mÅ)	log ϵ(X)
CH	4049.000	⋯	⋯	syn	6.73
CH	4246.000	⋯	⋯	syn	6.78
CH	4261.000	⋯	⋯	syn	6.73
CH	4280.000	⋯	⋯	syn	6.78
CH	4313.000	⋯	⋯	syn	6.71
C2	4737.000	⋯	⋯	syn	6.83
C2	4940.000	⋯	⋯	syn	6.78
C2	5165.000	⋯	⋯	syn	6.78
C I	8335.000	⋯	⋯	syn	6.78
NH	3360.000	⋯	⋯	syn	5.33
NH	3380.000	⋯	⋯	syn	5.33
CN	3883.000	⋯	⋯	syn	5.38
[O I]	6300.300	0.00	−9.820	syn	7.36
Na I	5889.950	0.00	0.108	138.08	3.40
Na I	5895.924	0.00	−0.194	114.15	3.24
Mg I	3829.355	2.71	−0.208	132.26	4.61
Mg I	3832.304	2.71	0.270	161.32	4.59
Mg I	4702.990	4.33	−0.380	31.11	4.53
Mg I	5172.684	2.71	−0.450	142.09	4.66
Mg I	5183.604	2.72	−0.239	151.64	4.62
Mg I	5528.405	4.34	−0.498	30.19	4.62
Al I	3961.520	0.01	−0.340	syn	2.70
Si I	4102.936	1.91	−3.140	syn	4.43
K I	7664.900	0.00	0.135	15.82	2.04
K I	7698.960	0.00	−0.168	10.57	2.15
Ca I	4454.780	1.90	0.260	42.23	3.15
Ca I	4455.890	1.90	−0.530	9.73	3.10
Ca I	5588.760	2.52	0.210	14.42	3.22
Ca I	5594.468	2.52	0.097	8.48	3.07
Ca I	5598.487	2.52	−0.087	6.78	3.16
Ca I	6102.720	1.88	−0.790	7.03	3.11
Ca I	6122.220	1.89	−0.315	21.52	3.21
Ca I	6162.170	1.90	−0.089	29.02	3.16
Ca I	6439.070	2.52	0.470	18.79	3.07
Sc II	4415.544	0.59	−0.670	42.74	−0.08
Sc II	5526.785	1.77	0.020	14.79	−0.06
Sc II	5657.907	1.51	−0.600	7.95	−0.06
Ti I	3989.760	0.02	−0.062	27.51	1.56
Ti I	3998.640	0.05	0.010	30.30	1.58
Ti I	4533.249	0.85	0.532	18.55	1.68
Ti I	4981.730	0.84	0.560	18.31	1.60
Ti I	4991.070	0.84	0.436	13.27	1.56
Ti II	3380.276	0.05	−0.630	106.63	1.66
Ti II	3383.759	0.00	0.160	135.11	1.70
Ti II	3489.736	0.14	−1.980	63.11	1.70
Ti II	3759.291	0.61	0.280	126.62	1.65
Ti II	3761.320	0.57	0.180	122.07	1.57
Ti II	3913.461	1.12	−0.420	82.78	1.58
Ti II	4012.396	0.57	−1.750	52.68	1.59
Ti II	4417.714	1.17	−1.190	47.45	1.60
Ti II	4418.331	1.24	−1.970	10.35	1.58
Ti II	4443.801	1.08	−0.720	76.06	1.56
Ti II	4450.482	1.08	−1.520	33.21	1.57
Ti II	4464.448	1.16	−1.810	22.62	1.72
Ti II	4468.517	1.13	−0.600	83.05	1.64
Ti II	4470.853	1.17	−2.020	11.60	1.60
Ti II	4501.270	1.12	−0.770	72.62	1.56
Ti II	4533.960	1.24	−0.530	82.19	1.67
Ti II	4563.770	1.22	−0.960	61.57	1.66
Ti II	4571.971	1.57	−0.320	73.45	1.67
Ti II	4589.915	1.24	−1.790	19.49	1.71
Ti II	5129.156	1.89	−1.240	12.80	1.68
Ti II	5188.687	1.58	−1.050	30.24	1.57

Table 3
(Continued)

Ion	λ (Å)	χ (eV)	log *gf*	EW (mÅ)	log ϵ (X)
Ti II	5226.538	1.57	−1.260	22.88	1.61
Ti II	5336.786	1.58	−1.590	13.81	1.68
Cr I	3578.680	0.00	0.420	84.88	1.75
Cr I	5206.040	0.94	0.020	31.85	1.75
Cr I	5208.419	0.94	0.160	38.08	1.72
Mn I	4041.380	2.11	−0.350	syn	1.43
Mn I	4754.021	2.28	−0.647	syn	1.48
Mn I	4783.424	2.30	−0.736	syn	1.48
Mn I	4823.514	2.32	−0.466	syn	1.48
Fe I	3476.702	0.12	−1.506	103.14	3.97
Fe I	3490.574	0.05	−1.105	120.06	3.99
Fe I	3565.379	0.96	−0.133	118.17	3.91
Fe I	3608.859	1.01	−0.090	120.76	3.95
Fe I	3618.768	0.99	−0.003	123.86	3.90
Fe I	3727.619	0.96	−0.609	110.58	3.93
Fe I	3743.362	0.99	−0.790	103.77	3.95
Fe I	3753.611	2.18	−0.890	37.23	3.81
Fe I	3758.233	0.96	−0.005	131.64	3.81
Fe I	3763.789	0.99	−0.221	124.07	3.90
Fe I	3765.539	3.24	0.482	46.35	3.85
Fe I	3767.192	1.01	−0.390	113.22	3.82
Fe I	3786.677	1.01	−2.185	47.17	3.92
Fe I	3787.880	1.01	−0.838	98.39	3.84
Fe I	3805.343	3.30	0.313	37.77	3.91
Fe I	3815.840	1.48	0.237	124.21	3.96
Fe I	3820.425	0.86	0.157	159.54	3.87
Fe I	3825.881	0.91	−0.024	143.00	3.88
Fe I	3827.823	1.56	0.094	110.35	3.87
Fe I	3840.438	0.99	−0.497	115.64	3.90
Fe I	3865.523	1.01	−0.950	95.35	3.82
Fe I	3887.048	0.91	−1.140	98.55	3.97
Fe I	3899.707	0.09	−1.515	118.38	4.00
Fe I	3917.181	0.99	−2.155	56.79	4.02
Fe I	3922.912	0.05	−1.626	114.89	3.96
Fe I	3940.878	0.96	−2.600	32.77	3.97
Fe I	3949.953	2.18	−1.251	25.93	3.91
Fe I	3977.741	2.20	−1.120	30.42	3.90
Fe I	4005.242	1.56	−0.583	93.96	4.02
Fe I	4021.866	2.76	−0.730	19.75	3.90
Fe I	4045.812	1.49	0.284	121.58	3.80
Fe I	4062.441	2.85	−0.860	16.32	4.03
Fe I	4063.594	1.56	0.062	112.62	3.87
Fe I	4067.978	3.21	−0.470	9.91	3.81
Fe I	4071.738	1.61	−0.008	109.82	3.92
Fe I	4076.629	3.21	−0.370	15.60	3.93
Fe I	4132.058	1.61	−0.675	81.69	3.81
Fe I	4134.678	2.83	−0.649	18.45	3.86
Fe I	4143.414	3.05	−0.200	22.46	3.77
Fe I	4143.868	1.56	−0.511	95.27	3.94
Fe I	4147.669	1.48	−2.071	22.83	3.81
Fe I	4152.169	0.96	−3.232	9.20	3.89
Fe I	4153.899	3.40	−0.320	11.21	3.93
Fe I	4156.799	2.83	−0.808	17.10	3.98
Fe I	4187.039	2.45	−0.514	43.23	3.81
Fe I	4191.430	2.47	−0.666	38.82	3.91
Fe I	4202.029	1.49	−0.689	86.91	3.79
Fe I	4216.184	0.00	−3.357	53.33	3.93
Fe I	4222.213	2.45	−0.914	28.52	3.92
Fe I	4227.427	3.33	0.266	34.77	3.89
Fe I	4233.603	2.48	−0.579	44.10	3.93
Fe I	4250.787	1.56	−0.713	90.86	3.98
Fe I	4260.474	2.40	0.077	79.14	3.88
Fe I	4383.545	1.48	0.200	132.48	3.99

Table 3
(Continued)

Ion	λ (Å)	χ (eV)	log *gf*	EW (mÅ)	log ϵ (X)
Fe I	4404.750	1.56	−0.147	107.01	3.81
Fe I	4415.122	1.61	−0.621	94.81	4.01
Fe I	4447.717	2.22	−1.339	24.49	3.97
Fe I	4459.118	2.18	−1.279	29.92	3.98
Fe I	4461.653	0.09	−3.194	66.31	4.08
Fe I	4466.552	2.83	−0.600	22.03	3.88
Fe I	4476.019	2.85	−0.820	15.62	3.94
Fe I	4489.739	0.12	−3.899	24.23	4.03
Fe I	4494.563	2.20	−1.143	32.40	3.92
Fe I	4528.614	2.18	−0.822	48.24	3.86
Fe I	4531.148	1.48	−2.101	29.24	3.96
Fe I	4592.651	1.56	−2.462	11.74	3.92
Fe I	4602.941	1.49	−2.208	28.74	4.06
Fe I	4871.318	2.87	−0.362	35.31	3.95
Fe I	4872.137	2.88	−0.567	25.69	3.97
Fe I	4890.755	2.88	−0.394	27.67	3.84
Fe I	4891.492	2.85	−0.111	44.87	3.85
Fe I	4903.310	2.88	−0.926	8.93	3.78
Fe I	4918.994	2.85	−0.342	31.74	3.83
Fe I	4920.503	2.83	0.068	51.65	3.77
Fe I	4994.130	0.92	−2.969	20.20	3.91
Fe I	5006.119	2.83	−0.615	24.99	3.93
Fe I	5012.068	0.86	−2.642	46.11	4.03
Fe I	5041.072	0.96	−3.090	17.32	4.00
Fe I	5041.756	1.49	−2.200	25.17	3.94
Fe I	5049.820	2.28	−1.355	21.12	3.93
Fe I	5051.634	0.92	−2.764	31.00	3.94
Fe I	5068.766	2.94	−1.041	8.17	3.92
Fe I	5083.339	0.96	−2.842	28.29	4.01
Fe I	5110.413	0.00	−3.760	42.15	4.04
Fe I	5127.360	0.92	−3.249	14.02	3.99
Fe I	5150.839	0.99	−3.037	17.36	3.98
Fe I	5166.282	0.00	−4.123	22.79	4.01
Fe I	5171.596	1.49	−1.721	50.65	3.93
Fe I	5191.455	3.04	−0.551	16.60	3.88
Fe I	5192.344	3.00	−0.421	23.33	3.89
Fe I	5194.942	1.56	−2.021	30.26	3.94
Fe I	5202.336	2.18	−1.871	10.87	3.98
Fe I	5216.274	1.61	−2.082	21.60	3.87
Fe I	5232.940	2.94	−0.057	42.19	3.84
Fe I	5266.555	3.00	−0.385	22.17	3.83
Fe I	5269.537	0.86	−1.333	108.24	3.97
Fe I	5281.790	3.04	−0.833	8.36	3.82
Fe I	5283.621	3.24	−0.524	14.25	4.01
Fe I	5302.300	3.28	−0.720	7.06	3.91
Fe I	5324.179	3.21	−0.103	25.16	3.85
Fe I	5328.039	0.92	−1.466	97.68	3.92
Fe I	5328.531	1.56	−1.850	41.23	3.97
Fe I	5332.900	1.55	−2.776	7.85	3.98
Fe I	5339.930	3.27	−0.720	8.47	3.98
Fe I	5371.489	0.96	−1.644	94.91	4.07
Fe I	5397.128	0.92	−1.982	82.11	4.07
Fe I	5405.775	0.99	−1.852	83.50	4.05
Fe I	5429.696	0.96	−1.881	85.76	4.09
Fe I	5434.524	1.01	−2.126	65.62	4.00
Fe I	5446.917	0.99	−1.910	81.57	4.07
Fe I	5455.609	1.01	−2.090	71.07	4.06
Fe I	5497.516	1.01	−2.825	24.49	3.95
Fe I	5506.779	0.99	−2.789	30.32	4.01
Fe I	5572.842	3.40	−0.275	12.52	3.87
Fe I	5586.756	3.37	−0.144	16.42	3.83
Fe I	5615.644	3.33	0.050	26.93	3.87
Fe I	6065.481	2.61	−1.410	8.79	3.88

Table 3
(Continued)

Ion	λ (Å)	χ (eV)	log *gf*	EW (mÅ)	log ϵ (X)
Fe I	6136.615	2.45	−1.410	17.74	4.03
Fe I	6137.691	2.59	−1.346	12.51	3.96
Fe I	6191.558	2.43	−1.416	14.18	3.90
Fe I	6230.723	2.56	−1.276	16.39	3.99
Fe I	6252.555	2.40	−1.687	8.74	3.90
Fe I	6393.601	2.43	−1.576	12.79	4.00
Fe I	6400.000	3.60	−0.290	7.57	3.84
Fe I	6430.846	2.18	−1.946	11.45	4.02
Fe I	6494.980	2.40	−1.239	23.26	3.93
Fe I	6677.986	2.69	−1.418	10.53	4.04
Fe II	4520.224	2.81	−2.600	9.38	3.92
Fe II	4555.890	2.83	−2.400	12.72	3.88
Fe II	4583.840	2.81	−1.930	35.22	3.96
Fe II	4923.930	2.89	−1.320	61.88	3.90
Fe II	5018.450	2.89	−1.220	69.87	3.94
Fe II	5197.580	3.23	−2.220	8.21	3.92
Fe II	5276.000	3.20	−2.010	15.34	3.98
Co I	3845.468	0.92	0.010	51.86	1.55
Co I	3995.306	0.92	−0.220	42.58	1.58
Co I	4121.318	0.92	−0.320	37.58	1.57
Ni I	3452.880	0.11	−0.900	85.60	2.48
Ni I	3483.770	0.28	−1.120	72.72	2.46
Ni I	3492.960	0.11	−0.265	107.58	2.50
Ni I	3500.850	0.17	−1.294	73.79	2.53
Ni I	3519.770	0.28	−1.422	64.22	2.50
Ni I	3524.540	0.03	0.007	122.09	2.47
Ni I	3597.710	0.21	−1.115	78.75	2.50
Ni I	3783.520	0.42	−1.420	65.82	2.55
Ni I	3807.140	0.42	−1.220	69.61	2.43
Ni I	5476.900	1.83	−0.890	17.68	2.52
Sr II	4077.714	0.00	0.150	syn	−1.23
Sr II	4215.524	0.00	−0.180	syn	−1.28
Y II	5205.731	1.03	−0.340	syn	−1.64
Zr II	3998.965	0.56	−0.520	syn	−1.20
Zr II	4045.613	0.71	−0.860	syn	−0.97
Ru I	3728.025	0.00	0.260	syn	−1.20
Pd I	3404.579	0.81	0.320	syn	−1.43
Ba II	4554.033	0.00	0.163	syn	−0.97
Ba II	4934.086	0.00	−0.160	syn	−1.02
Ba II	5853.680	0.60	−2.560	syn	−1.12
Ba II	6141.710	0.70	−0.008	syn	−1.04
Ba II	6496.896	0.60	−0.369	syn	−1.07
La II	3995.740	0.17	−0.686	syn	−2.10
La II	4086.710	0.00	−0.696	syn	−2.15
Ce II	4053.503	0.00	−0.610	syn	−1.57
Pr II	4179.475	0.20	−0.194	syn	−2.28
Pr II	4222.934	0.05	−0.557	syn	−2.43
Nd II	4012.700	0.00	−0.600	syn	−1.88
Nd II	4043.590	0.32	−0.710	syn	−1.88
Nd II	4061.080	0.47	0.550	syn	−1.98
Sm II	4318.930	0.28	−0.250	syn	−2.04
Sm II	4424.334	0.48	0.140	syn	−2.34
Sm II	4642.230	0.38	−0.460	syn	−2.09
Eu II	3724.934	0.00	−0.855	syn	−2.38
Eu II	4435.457	0.21	−0.696	syn	−2.33
Gd II	3549.360	0.24	0.290	syn	−1.93
Gd II	4251.730	0.38	−0.220	syn	−2.08
Dy II	3536.020	0.54	0.53	syn	−1.80
Dy II	4077.970	0.10	−0.04	syn	−2.10
Ho II	3456.010	0.00	0.76	syn	−2.52
Ho II	3890.970	0.08	0.46	syn	−2.67
Er II	3692.650	0.06	0.28	syn	−2.18
Er II	3729.520	0.00	−0.59	syn	−2.08

Table 3
(Continued)

Ion	λ (Å)	χ (eV)	log *gf*	EW (mÅ)	log ϵ (X)
Er II	3906.310	0.00	0.12	syn	−2.18
Tm II	3462.200	0.00	0.03	syn	−2.85
Yb II	3694.195	0.00	−0.300	syn	−2.46
Pb I	4057.814	1.32	−0.220	syn	<0.30
Th II	4019.129	0.00	−0.650	syn	<−2.20

(This table is available in its entirety in machine-readable form.)

Table 4
Abundances for Individual Species

Species	log $\epsilon_{\odot}$(X)	log ϵ (X)	[X/H]	[X/Fe]	σ	*N*
C	8.43	6.76	−1.67	+1.90	0.10	6
C [a]	8.43	7.20	−1.23	+2.34	0.10	6
N	7.83	5.35	−2.48	+1.09	0.15	3
O I	8.69	7.36	−1.34	+2.24	0.10	1
Na I	6.24	3.32	−2.92	+0.65	0.15	2
Mg I	7.60	4.60	−3.00	+0.58	0.10	6
Al I	6.45	2.70	−3.75	−0.18	0.15	1
Si I	7.51	4.43	−3.08	+0.49	0.15	1
K I	5.03	2.10	−2.93	+0.64	0.10	2
Ca I	6.34	3.14	−3.20	+0.37	0.10	9
Sc II	3.15	−0.07	−3.22	+0.36	0.10	3
Ti I	4.95	1.60	−3.35	+0.22	0.10	5
Ti II	4.95	1.63	−3.32	+0.25	0.10	23
Cr I	5.64	1.74	−3.90	−0.33	0.10	3
Mn I	5.43	1.47	−3.96	−0.39	0.10	4
Fe I	7.50	3.93	−3.57	0.00	0.10	127
Fe II	7.50	3.93	−3.57	0.00	0.10	7
Co I	4.99	1.57	−3.42	+0.15	0.10	3
Ni I	6.22	2.49	−3.73	−0.16	0.10	10
Sr II	2.87	−1.26	−4.13	−0.56	0.20	2
Y II	2.21	−1.64	−3.85	−0.28	0.20	1
Zr II	2.58	−1.09	−3.67	−0.10	0.25	2
Ru I	1.75	−1.20	−2.95	+0.62	0.25	1
Pd I	1.57	−1.43	−3.00	+0.57	0.25	1
Ba II	2.18	−1.04	−3.22	+0.35	0.15	5
La II	1.10	−2.13	−3.23	+0.34	0.20	2
Ce II	1.58	−1.57	−3.15	+0.42	0.20	1
Pr II	0.72	−2.36	−3.08	+0.49	0.30	2
Nd II	1.42	−1.91	−3.33	+0.24	0.20	3
Sm II	0.96	−2.16	−3.12	+0.45	0.30	3
Eu II	0.52	−2.36	−2.88	+0.69	0.20	2
Gd II	1.07	−2.00	−3.07	+0.50	0.25	2
Dy II	1.10	−1.95	−3.05	+0.52	0.20	3
Ho II	0.48	−2.60	−3.08	+0.49	0.20	2
Er II	0.92	−2.15	−3.07	+0.50	0.20	3
Tm II	0.10	−2.85	−2.95	+0.62	0.25	1
Yb II	0.84	−2.46	−3.30	+0.27	0.25	1
Pb I	1.75	<0.30	<−1.45	<+2.12	⋯	1
Th II	0.02	<−2.20	<−2.22	<+1.35	⋯	1

Note.
[a] Using the carbon evolutionary corrections of Placco et al. (2014c).

The top panel of Figure 2 shows the spectral synthesis of the CH *G*-band at λ4280 for RAVE J1830−4555. The points represent the observed spectrum, the solid blue line is the best abundance fit, and the shaded area represents a variation of

Table 5
Example Systematic Abundance Uncertainties for RAVE J1830−4555

Element	$\Delta T_{\rm eff}$ +150 K	$\Delta\log g$ +0.3 dex	$\Delta\xi$ +0.3 km s^{-1}	$\sigma/\sqrt{n}$	$\sigma_{\rm tot}$
O I	0.12	0.05	−0.00	0.10	0.17
Na I	0.18	−0.04	−0.11	0.07	0.23
Mg I	0.14	−0.05	−0.07	0.04	0.17
Al I	0.17	−0.05	−0.12	0.10	0.24
Si I	0.16	−0.01	−0.01	0.10	0.19
K I	0.12	−0.01	−0.00	0.07	0.14
Ca I	0.10	−0.01	−0.01	0.03	0.11
Sc II	0.08	0.05	−0.01	0.06	0.11
Ti I	0.17	−0.01	−0.01	0.04	0.18
Ti II	0.10	0.04	−0.07	0.02	0.13
Cr I	0.19	−0.03	−0.06	0.06	0.21
Mn I	0.21	−0.02	−0.05	0.07	0.23
Fe I	0.17	−0.02	−0.06	0.01	0.18
Fe II	0.03	0.06	−0.02	0.04	0.08
Co I	0.19	−0.01	−0.03	0.06	0.20
Ni I	0.24	−0.05	−0.12	0.03	0.27
Sr II	0.13	0.04	−0.13	0.07	0.20
Ba II	0.16	0.03	−0.14	0.10	0.24

±0.1 dex in abundance, used to estimate the uncertainty. The gray line shows the synthesized spectrum in the absence of carbon. The lower panel shows the residuals (in %) between the observed data and the best fit, which are all below 10% for the synthesized region. As RAVE J1830−4555 is on the upper red giant branch, the observed carbon abundance does not reflect the chemical composition of its natal cloud. We determined the carbon depletion due to CN processing for RAVE J1830−4555 to be 0.44 dex, by using the online calculator[24] described in Placco et al. (2014b).

The $^{12}C/^{13}C$ isotopic ratio is an indicator of the extent of mixing processes on the red giant branch stage of evolution. Using a fixed carbon abundance of $\log\epsilon(C) = 6.76$ for the CH features at λ4217, we derived $^{12}C/^{13}C = 17 \pm 4$, suggesting that substantial processing of ^{12}C into ^{13}C has taken place in RAVE J1830−4555. The lower left panel of Figure 2 show the determination of the $^{12}C/^{13}C$ isotopic ratio and its uncertainty. Note that the residuals between the observed data and $^{12}C/^{13}C = 17$ are all within 3%. For the remainder of the analysis, we have fixed the carbon abundance ($\log\epsilon(C) = 6.76$) and isotopic ratio ($^{12}C/^{13}C = 17$), which is of particular importance for stars with such high levels of carbon as RAVE J1830−4555.

The nitrogen abundance was determined from spectral synthesis of the NH band at λ3360 ($\log\epsilon(N) = 5.33$) and the CN band at λ3883 ($\log\epsilon(N) = 5.38$). For the CN band, we used a fixed carbon abundance as explained above. Individual determinations agree within 0.05 dex and the final average abundance is $\log\epsilon(N) = 5.35$ ([N/Fe] = +1.09). The middle panel of Figure 2 shows the spectral synthesis for the NH region at λ3360. Similar to carbon, the shaded area (encompassing ±0.2 dex from the best fit) successfully describes the behavior of this region.

The lower right panel of Figure 2 shows the synthesis for the forbidden oxygen transition at λ6300. Due to the relatively high S/N of the MIKE spectrum in this region, we were able to determine an abundance of $\log\epsilon(O) = 7.36$ ([O/Fe] = +2.24) with an uncertainty of 0.1 dex. Both carbon and nitrogen abundances were determined assuming $\log\epsilon(O) = 7.36$ for the synthetic spectra.

[24] http://vplacco.pythonanywhere.com/

4.2. From Sodium to Nickel

Abundances of Na, Mg, K, Ca, Sc, Ti, Cr, Co, and Ni were determined by equivalent-width analysis only. For Ti, we were able to measure transitions from two different ionization stages; the abundances agree within 0.03 dex. For Al, Si, and Mn, spectral synthesis was used to determine the abundances. Individual line measurements are listed in Table 3 and final average abundances are listed in Table 4. Figure 3 shows the comparison between the light-element abundances (from C to Ni), as a function of the metallicity, for RAVE J1830−4555 and stars in the JINAbase compilation (Abohalima & Frebel 2018).[25] Apart from the notably high carbon and oxygen abundances, the measurements for RAVE J1830−4555 are within the general trends for its metallicity range. In Section 5.2 we explore the main characteristics of the possible progenitor population of RAVE J1830−4555, which could help explain its light-element abundance pattern.

4.3. Neutron-capture Elements

The chemical abundances for 20 neutron-capture elements (from Sr to Th) were measured in the spectrum of RAVE J1830−4555 through spectral synthesis. We have used the atomic and molecular line lists generated by the `linemake` code.[26] Individual references for transitions are given in their README file. Where appropriate, we accounted for line broadening by hyperfine splitting structure and isotopic shifts. As stated above, for all syntheses we fixed the abundances of carbon and nitrogen, and the $^{12}C/^{13}C$ ratio. We also used the *r*-process isotopic fractions from Sneden et al. (2008) for specific elements, as described below. Individual line measurements can be found in Table 3 and final average abundances in Table 4.

Figure 4 shows a comparison between the neutron-capture element abundances (from Sr to Th), as a function of the metallicity, for RAVE J1830−4555 and stars in the JINAbase compilation (Abohalima & Frebel 2018). Similar to the light elements, RAVE J1830−4555 appears to follow the general trends shown by the literature data. However, it is interesting to note that RAVE J1830−4555 is among the stars with the lowest metallicity for which elements heavier than barium ($Z = 56$) have ever been measured.[27] In the following, we provide details on the determinations of neutron-capture element abundances and upper limits.

Strontium, yttrium, zirconium—These elements belong to the first *r*-process peak and are believed to be formed by the limited *r*-process (Frebel 2018). The upper left panel of Figure 5 shows the spectral synthesis for the Sr λ4077 absorption feature. The abundance found for this line ($\log\epsilon(Sr) = -1.23$) agrees well with the value found for the λ4215 line ($\log\epsilon(Sr) = -1.28$). For Y, we were only able to measure one feature (λ5205: $\log\epsilon(Y) = -1.64$), which lies on the blue wing of a well-modeled Cr feature. For Zr, two lines

[25] The values were scaled using the solar photospheric abundances of Asplund et al. (2009).
[26] https://github.com/vmplacco/linemake
[27] Other examples of stars with Eu detected include CS 22891−200 ([Fe/H] = −3.9; Roederer et al. 2014a) and SMSS J0248−6843 ([Fe/H] = −3.7; Jacobson et al. 2015).

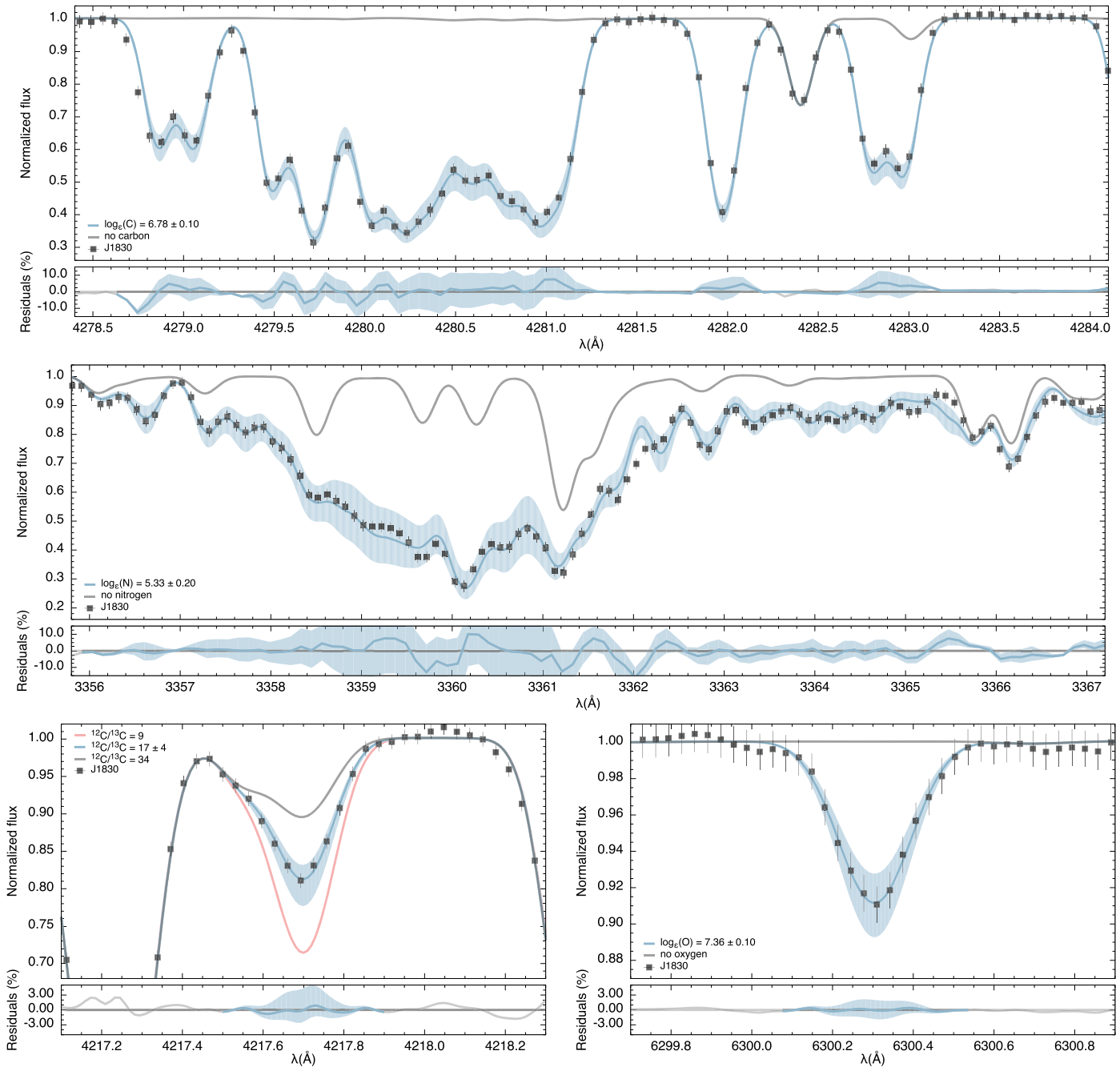

Figure 2. Spectral syntheses for the determination of the abundances of carbon (upper panel), nitrogen (middle panel), and oxygen (lower right panel). The top panel of each plot shows the best-fit syntheses (blue lines) and uncertainties (shaded regions) compared to the observed spectra (points). Also shown are syntheses after removing all the contributions from specific elements (gray lines). The bottom panels show the residuals between the observed spectra and the syntheses. The lower left panel shows the determination of the $^{12}C/^{13}C$ ratio (see text for details).

were measured: λ3998 ($\log\epsilon\,(\mathrm{Zr}) = -1.20$) and λ4045 ($\log\epsilon\,(\mathrm{Zr}) = -0.97$), with abundances agreeing within 1σ.

Ruthenium, palladium. These elements are part of the less explored region within $41 \leqslant Z \leqslant 55$. Abundances for these elements are challenging to measure, and successful determinations are mostly made in the near-ultraviolet range (e.g., Roederer et al. 2012, among others). From the MIKE spectrum we were able to measure one Ru feature (λ3728: $\log\epsilon\,(\mathrm{Ru}) = -1.20$) and one Pd feature ($\lambda$3404: $\log\epsilon\,(\mathrm{Pd}) = -1.43$).

Barium, lanthanum. These elements are the main representatives of the second peak of the *s*-process. For Ba, abundances were determined from five lines, with an average abundance of $\log\epsilon\,(\mathrm{Ba}) = -1.04$, agreeing within 0.15 dex. In all cases, we have accounted for the Ba isotopic fractions, following Sneden et al. (2008). The upper right panel of Figure 5 shows the synthesis for the Ba λ6496 line, where the shaded area represents an abundance variation of $\pm$0.10 dex. For La, we were able to identify two lines (λ3995 and λ4086) in regions

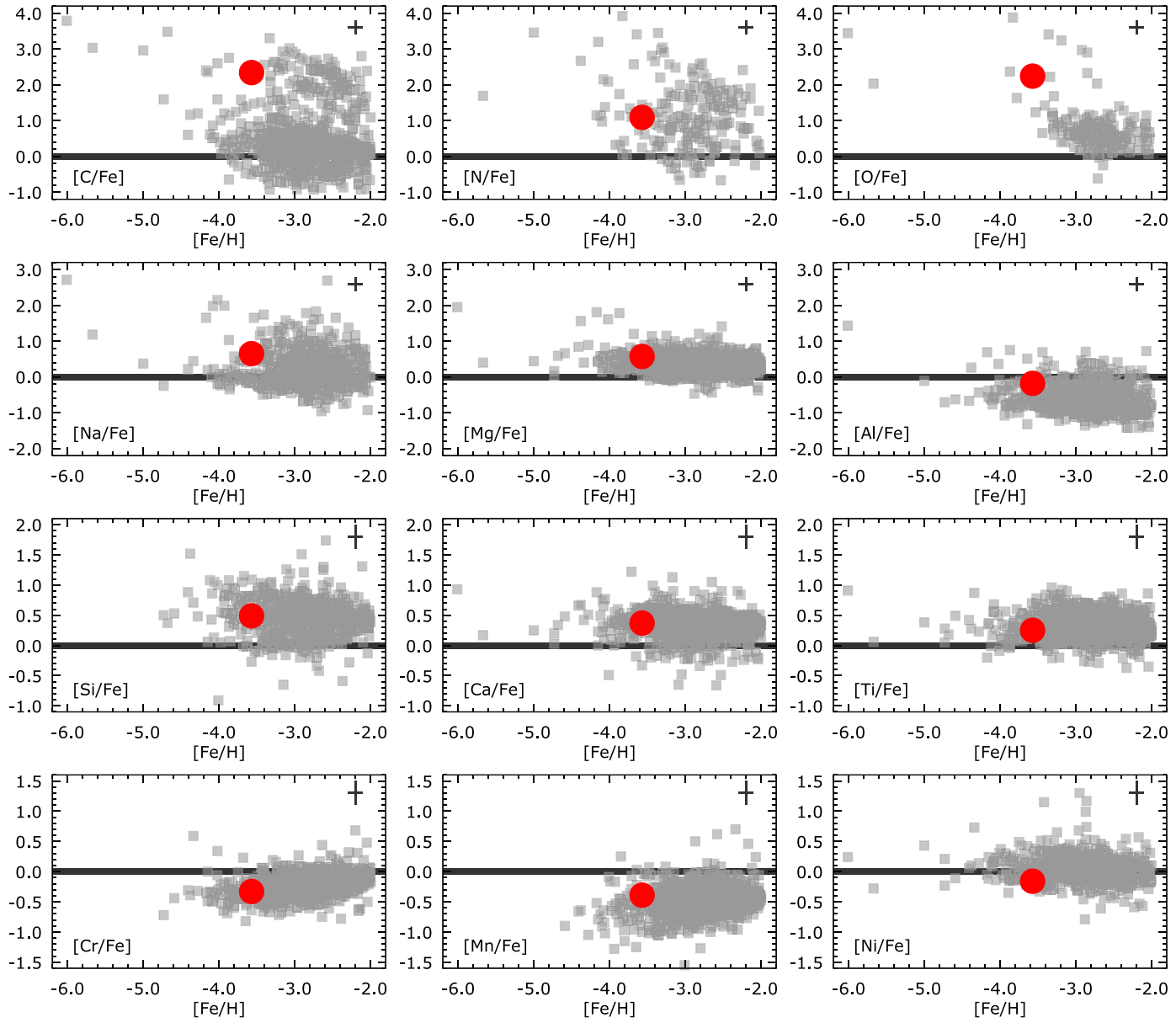

Figure 3. Light-element abundance ratios, as a function of the metallicity, for RAVE J1830−4555 (red filled circle) and the JINAbase literature compilation (Abohalima & Frebel 2018).

less affected by blends and carbon features, with an average abundance of $\log \epsilon$ (La) $= -2.13$.

Cerium, praseodymium, neodymium, samarium. A total of nine lines were used to determine the abundances of these elements. The agreement is within 1σ for Pr (two lines—0.15 dex) and Nd (three lines—0.10 dex), and 2σ for Sm (three lines—0.30 dex). Only one line was used to determine the abundance of Ce, with an uncertainty of 0.20 dex.

Europium. Europium is an important indicator of the *r*-process and has been widely used to distinguish between the various subclasses of neutron-capture enhanced metal-poor stars. In the solar system, Eu is mainly formed by the *r*-process (97%, according to Burris et al. 2000), and there are many strong absorption features that can be measured in the optical wavelength regime. Unfortunately, most Eu lines (notably λ4129 and λ4205) were within regions with strong molecular carbon absorption features, and hence could not be properly synthesized. We were able to measure abundances for two lines (λ3724 and λ4435) with an average abundance of $\log \epsilon$ (Eu) $= -2.36$. The middle left panel of Figure 5 shows the synthesis of the Eu λ3724 line. It is possible to see that the neighboring Fe line on the blue side of the Eu feature is well modeled, and the residuals confirm the good agreement between synthesis and observations.

Gadolinium, dysprosium, holmium, erbium, thulium, ytterbium. These elements are in the range $64 \leqslant Z \leqslant 70$ and have *r*-process fractions of at least 70% (Burris et al. 2000). All of the absorption features measured in the MIKE spectrum are in the blue region ($\lambda \leqslant 4200$ Å). The agreement between individual line measurements is within 1σ for Gd (two lines—0.15 dex), Ho (two lines—0.15 dex), and Er (three lines—0.10 dex), and within 2σ for Dy (two lines—0.30 dex). Only one line was measured for both Tm and Yb, with uncertainties of 0.25 dex. The top left and middle right panels of Figure 5

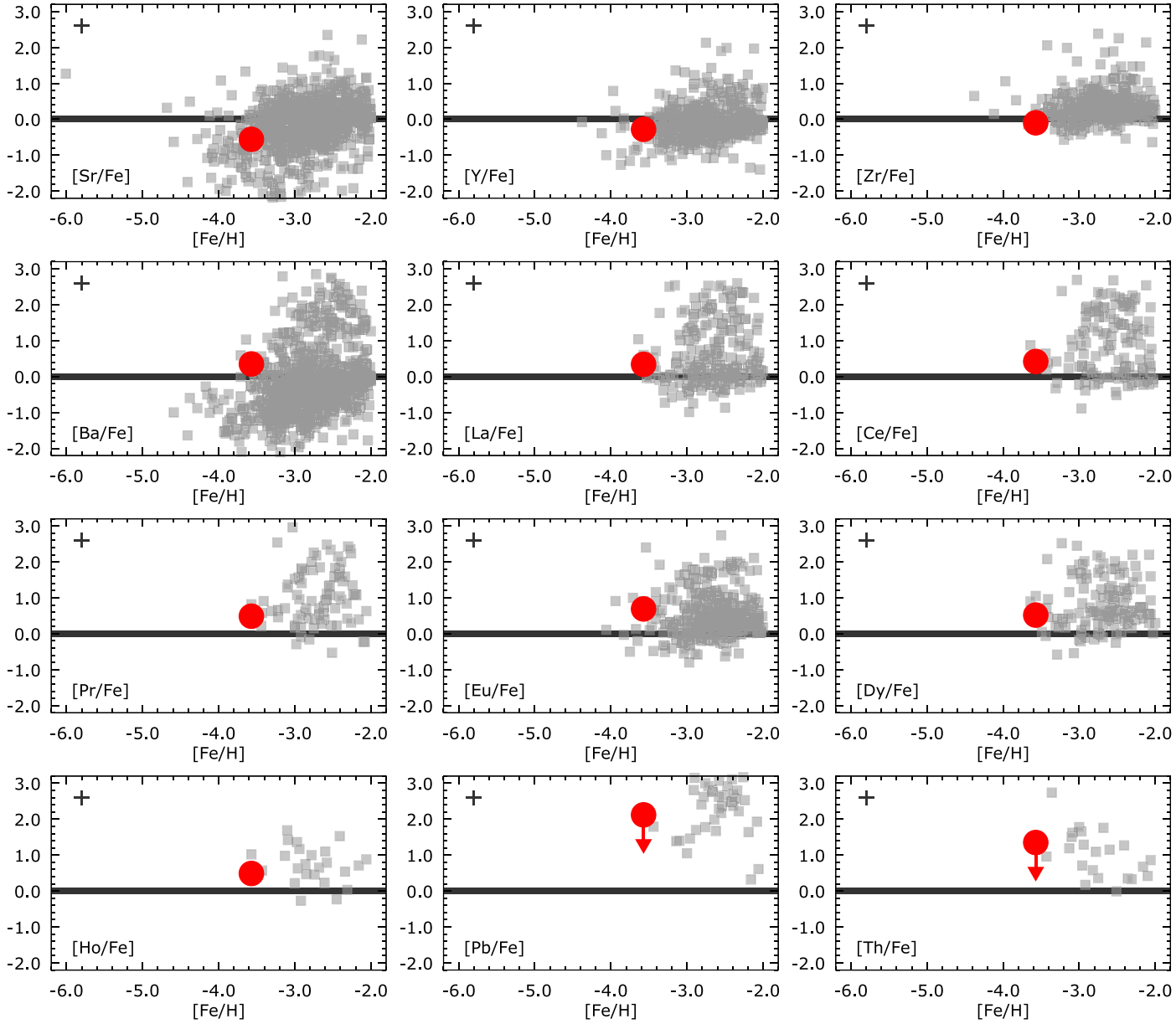

Figure 4. Neutron-capture element abundance ratios, as a function of the metallicity, for RAVE J1830−4555 (red filled circle) and the JINAbase literature compilation (Abohalima & Frebel 2018).

show, respectively, the spectral synthesis for Dy and Er. In both cases, there is a good agreement between the observations and best-fit abundances, with residuals within 3%.

Lead. Pb is a third-peak element typically produced by the *s*-process. However, at metallicities of [Fe/H] $\leqslant -3.5$, Pb is expected to be produced by the *r*-process by the same α-decay chains as thorium and uranium (Wanajo et al. 2002). Even the high S/N ratio of the MIKE spectrum did not allow for an abundance determination from the weak Pb line at λ4057, which is blended with a strong carbon feature (see below). We were able to place an upper limit on the Pb abundance. The lower left panel of Figure 5 shows the synthesis of the lead feature and also identifies other species that contribute to the observed absorption. For the best-fit and uncertainty determinations (blue solid line and blue shaded region), the abundances of C, N, Mg, Ca, V, and Mn were fixed based on results shown in Table 4, and the isotopic fractions were taken from Sneden et al. (2008). The gray and red solid lines show, respectively, syntheses with no contribution of lead and with a lead abundance that is 0.4 dex higher than the best fit, which we consider to be our upper limit. To further assess possible sources of contamination, we varied the abundance of carbon by 1σ (yellow shaded region). It is possible to see that any change in carbon would directly affect the blue side of the absorption feature centered at ∼4057.7 Å. Our final value for the lead abundance is $\log \epsilon\,(\mathrm{Pb}) < +0.30$.

Thorium. Th is a radioactive actinide, and the second heaviest element observable in stellar spectra. We were able to determine an upper limit for the Th abundance from one absorption feature at λ4019. Results are shown in the lower right panel of Figure 5. Similar to the Pb determination, we fixed the abundances of C, N, Fe, Co, Ni, Ce, and Nd before attempting to fit the Th feature. We also explored how changes in the carbon abundance affect the line strengths; results suggest that, even though C can be well constrained by the feature to the blue side of the Th line,

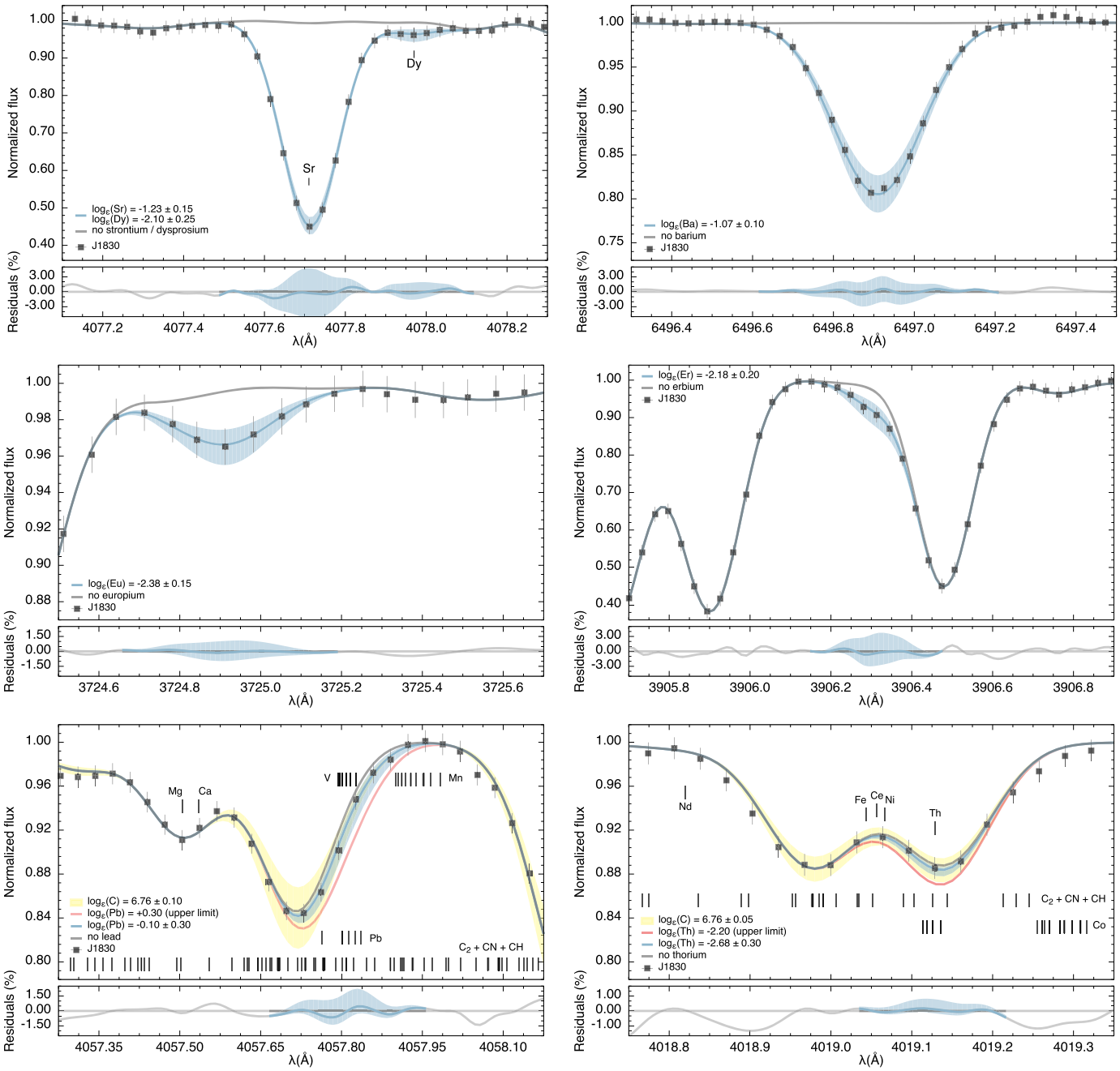

Figure 5. Same as Figure 2, but for neutron-capture elemental abundance determinations.

only an upper limit can be determined. Our final value is $\log \epsilon\,(\mathrm{Th}) < -2.20$.

5. Analysis

RAVE J1830−4555 has an intriguing chemical abundance pattern. The light elements present similar behavior to those of CEMP-no stars, while the heavy elements resemble the abundance pattern of an *r*-I star. In addition, a binary scenario does not appear to be a possibility due to the lack of appreciable radial-velocity variations. As a consequence, the chemical makeup of RAVE J1830−4555 requires an interstellar cloud pre-enriched with elements ranging from carbon to thorium. Below we speculate on the possible pathways that may have led to this scenario.

5.1. Radial-velocity Variations

The binary fractions among the different subclasses of low-metallicity stars have been subject to extensive study in the literature. Hansen et al. (2011) found that only three of their sample of 17 *r*-process enhanced stars were in binary systems. A follow-up study with additional radial-velocity data (Hansen et al. 2015) confirmed the conclusion that the chemical peculiarities of *r*-I and *r*-II stars are not caused by binary companions. In addition, about 83% of the CEMP-no stars do not present radial-velocity variations consistent with a binary system (Hansen et al. 2016b).

Due to its low metallicity and chemical abundance pattern (light elements commensurate with the CEMP-no class and neutron-capture elements with the *r*-I class), RAVE

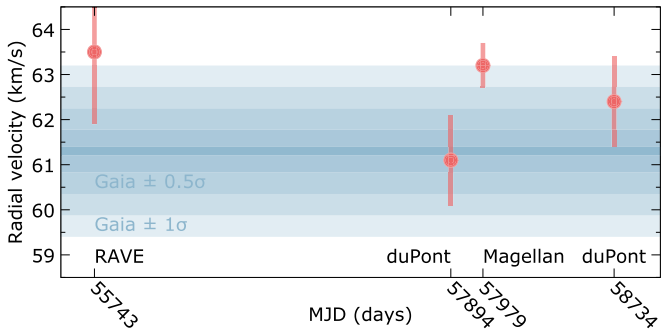

Figure 6. Radial velocities for RAVE J1830−4555 as a function of observation date. The solid line and shaded areas show, respectively, the Gaia average value (based on four measurements) and its uncertainty.

J1830−4555 would not be expected to belong to a binary system. The star HE 1012−1540 (Cohen et al. 2008) presents a similar case. It is a single EMP star ([Fe/H] ~ -3.5) with CNO enhancement and is mildly enhanced in neutron-capture elements ([Ba/Fe] $= +0.20$: Cohen et al. 2013; and [Ba/Fe] $= +0.07$: Roederer et al. 2014b).

The expectation that RAVE J1830−4555 is a single star is supported[28] by the radial-velocity (RV) measurements listed in Table 1. Furthermore, the uncertainty from the Gaia value (based on four epochs—Gaia DR2 does not provide individual RV measurements) is similar to the uncertainties for the other spectroscopic values. Figure 6 shows the individual measurements as a function of the observation date. The Gaia DR2 average value is shown as a solid line, with its uncertainty given by the shaded areas.

To further test the non-binary hypothesis, we made a comparison between the standard deviation of the Gaia measurement for RAVE J1830−4555 and stars with similar magnitudes ($G \pm 0.05$ mag, $G_{BP} \pm 0.05$ mag, and $G_{RP} \pm 0.05$ mag) and temperatures ($T_{eff} \pm 100$ K) present in the Gaia DR2 database. By inspecting the RV standard deviations for this subsample of stars, it is expected that binary stars would show characteristically larger values, while single stars (with similar parameters) would have similar RV dispersions.

In total, we found 7673 stars in the Gaia DR2 database that fulfill the magnitude and temperature constraints presented above. To calculate the standard deviation of the epoch radial velocities $\sigma(V_{rad}^t)$, we used the following relation[29]:

$$\sigma(V_{rad}^t) = \sqrt{\left(\frac{2 \times \texttt{o\_RV}}{\pi}\right) \times (\texttt{e\_RV}^2 - 0.11^2)}, \quad (1)$$

where `o_RV` is the number of epochs used to compute the radial velocity (`rv_nb_transits`) and `e_RV` is the radial-velocity error (`radial_velocity_error`). A constant noise floor of 0.11 km s^{-1} is added in quadrature to take into account calibration contributions.

Figure 7 shows the distribution of RV standard deviations for all stars (red histogram) and also for stars with four radial-velocity epochs measured (blue histogram), which is the case for RAVE J1830−4555. The labels on the figure show the number of stars, average, and standard deviation for $\sigma(V_{rad}^t)$ in both cases. The extended tails of the distributions are strong evidence of the presence of binaries. RAVE J1830−4555 has a value consistent with the average for both distributions, which adds confidence to the assertion of its non-binary status.

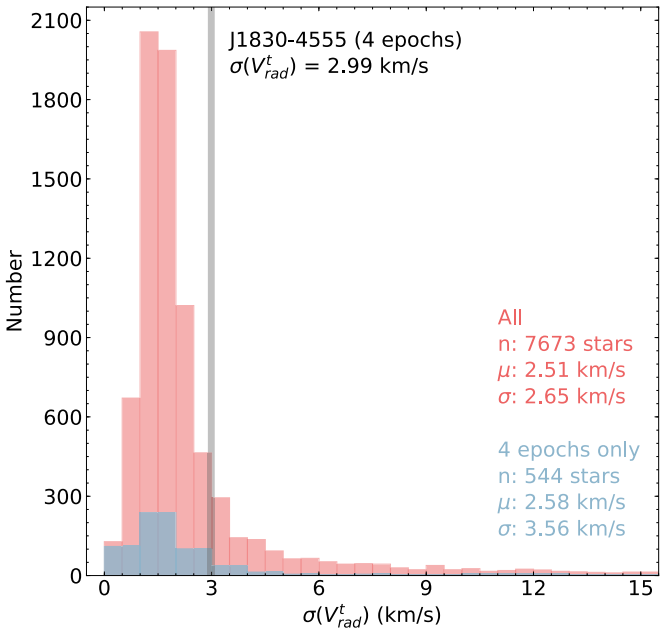

Figure 7. Distribution of radial-velocity standard deviations for stars in the Gaia DR2 database with similar temperatures and magnitudes to RAVE J1830−4555 (see text for details). The number of objects, mean, and standard deviation of the distribution are listed. The vertical solid line marks the $\sigma(V_{rad}^t)$ value for RAVE J1830−4555 .

5.2. The Light-element Abundance Pattern

At [Fe/H] $= -3.57$, RAVE J1830−4555 is well within the realm of the so-called mono-enriched stars, for which interstellar clouds were polluted by a single progenitor population (Hartwig et al. 2018). One of the main diagnostics to identify mono-enriched stars, along with [Fe/H], is the [Mg/C] abundance ratio. In the case of RAVE J1830−4555, both the observed and "natal" values ([Mg/C] $= -1.32$ and -1.76, respectively) are consistent with that classification (Figure 11 of Hartwig et al. 2018). Even though we argue in later sections that RAVE J1830−4555 could have been formed from a gas cloud polluted by more than one progenitor, here we speculate on the possible origin of the light elements, from carbon to nickel, from a single progenitor.

We attempted to model the light-element abundance signature of RAVE J1830−4555 with theoretical nucleosynthesis yields from Population III supernova[30] by Heger & Woosley (2010). These models follow the evolution and explosion of metal-free stars, where the initial composition is pristine Big Bang nucleosynthesis and both mass loss and rotation are neglected throughout the evolution. The (S4) fallback models have masses from 10 to 100 $M_\odot$ and explosion energies from 0.3×10^{51} erg to 10×10^{51} erg. Details of their χ^2 matching algorithm can be found in Placco et al. (2015, 2016a, 2016b) and Frebel & Norris (2015), where this procedure is applied to EMP stars in the literature.

[28] We also acknowledge the possibility that a lack of observed orbital motion for RAVE J1830−4555 could be due to the system's orientation (e.g., face-on) or a very long period ($P_{orb} \gtrsim 10$ yr).

[29] Derived from the equations provided in Table 14.1.1 of https://gea.esac.esa.int/archive/documentation/GDR2/.

[30] http://starfit.org

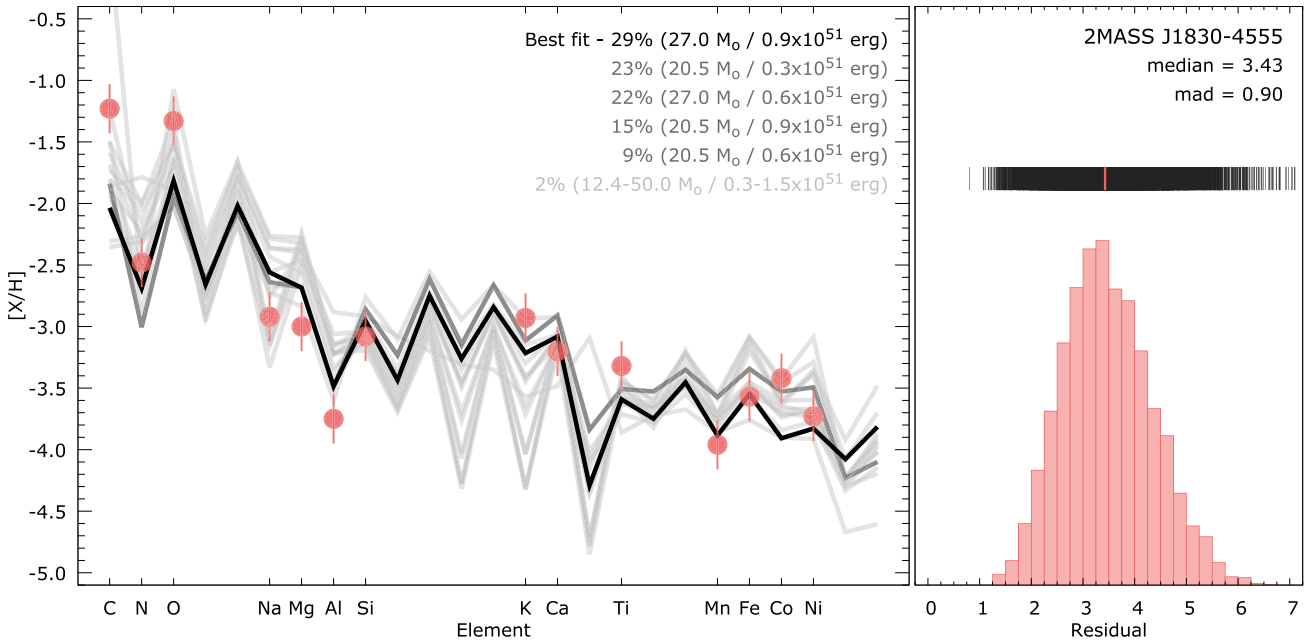

Figure 8. Best model fits for RAVE J1830−4555, ordered by increasing median residuals. The left panel shows the observed [X/H] abundance ratios (red filled circles), along with the yields (solid lines) from the S4 models described in Heger & Woosley (2010). The masses and explosion energies are provided in the legend at the upper right, color-coded by their fractional occurrence. The right panel shows the distribution of the residuals (in dex) for the 10,000 simulations (see text for details). The colored bar overlaying the upper density distribution in the right panel marks the median value, shown in the legend at the top right, along with the median absolute deviation (MAD).

The fitting results are shown in Figure 8. Similar[31] to Placco et al. (2016b), we generated 10,000 abundance patterns[32] for RAVE J1830−4555, by resampling the $\log \epsilon$ (X) and σ values from Table 4. By running the FIG8 code for each resampled pattern (and determining its respective best-fit model), we found that only 16 different models were used. Their fractions can be seen in the left panel of Figure 8. The "best-fit" result found in 29% of the resamples is a model with 27.0 $M_\odot$ and 0.9×10^{51} erg. In general, Figure 8 shows that a possible progenitor for RAVE J1830−4555 could have had a mass of 20.5–27 $M_\odot$ and an explosion energy of (0.3–0.9) $\times 10^{51}$ erg. This support the conclusion presented in Mardini et al. (2019b), which suggests that stellar masses $\sim$20 $M_\odot$ may reflect the initial mass function of the first stars. The right panel of Figure 8 shows the distribution of the residuals for each best-fit model. Comparing the median residual[31] (3.43) with the values for the ultra-metal-poor stars presented in Figure 3 of Placco et al. (2016b) confirms that RAVE J1830−4555 likely belongs to the group of stars for which the faint-supernova models of Heger & Woosley (2010) can explain the observed light-element abundances.

5.3. The Heavy-element Abundance Pattern

5.3.1. Comparison with Solar System r- and s-process Fractions

According to the classifications proposed by Beers & Christlieb (2005) and Frebel (2018), the heavy-element abundance pattern of RAVE J1830−4555 has a signature of the *main r-process* and it is classified as an *r*-I star ([Eu/Fe] = +0.69 and [Ba/Eu] = −0.34). The upper panel of Figure 9 shows the heavy-element abundance pattern of RAVE J1830−4555, compared to the solar system *r*-process (scaled to Eu) and *s*-process (scaled to Ba), using the fractions of Burris et al. (2000). Each label shows the element name and its *r* and *s* fractions in the Sun. The lower panel shows the residuals between observations and the *r* and *s* scaled patterns. The red shaded area denotes the typical uncertainty ($\sim$0.2 dex) in the abundance measurements.

It is possible to see that the elements from Pr to Yb reproduce the normalized *r*-process pattern quite well, within 1σ. The same applies to the lighter elements Ru and Pd. In contrast, the first-peak elements (Sr, Y, and Zr) appear to be underproduced when compared with the scaled patterns. Under the assumption that all the neutron-capture elements in J1830–4555 were produced by a single merger of neutron stars, we can estimate the lanthanide fraction that would be measured if we were to observe this merger's kilonova directly. Following the methods in Ji et al. (2019), we estimate the lanthanide fraction to be $\log X_{\rm La} = -1.47$. This lanthanide fraction is in the $\sim$80th percentile of lanthanide fractions for all stars and is higher than the lanthanide fraction observed in GW170817. For Ba, La, and Ce, there is a clear overproduction when compared to the scaled *r*-process pattern,[32] which could suggest a contribution of the *s*-process to the observed abundance pattern of RAVE J1830−4555.

The operation of the *s*-process can also be traced by abundance ratios such as [Ba/Eu], [La/Eu], and [Pb/Eu]. The traditional limit for *r*-process enhanced stars set by Beers & Christlieb (2005) is [Ba/Eu] < 0, which is met in the case of RAVE J1830−4555. In addition, Roederer et al. (2010) sets approximate minimum ratios expected from AGB pollution to be [La/Eu] $\approx$ 0.0 and [Pb/Eu] $\approx$ +0.3 (see their Figure 3 and also Figure 15 of Placco et al. 2013). For RAVE J1830−4555, the [La/Eu] ratio is consistent with the *r*-process expectation

[31] The residual for each iteration is taken as the sum of the absolute values of the differences between predicted yields and measurements.
[32] The *r*-process abundance pattern is derived by subtracting the *s*-process contributions from the solar system values (Roederer et al. 2010).

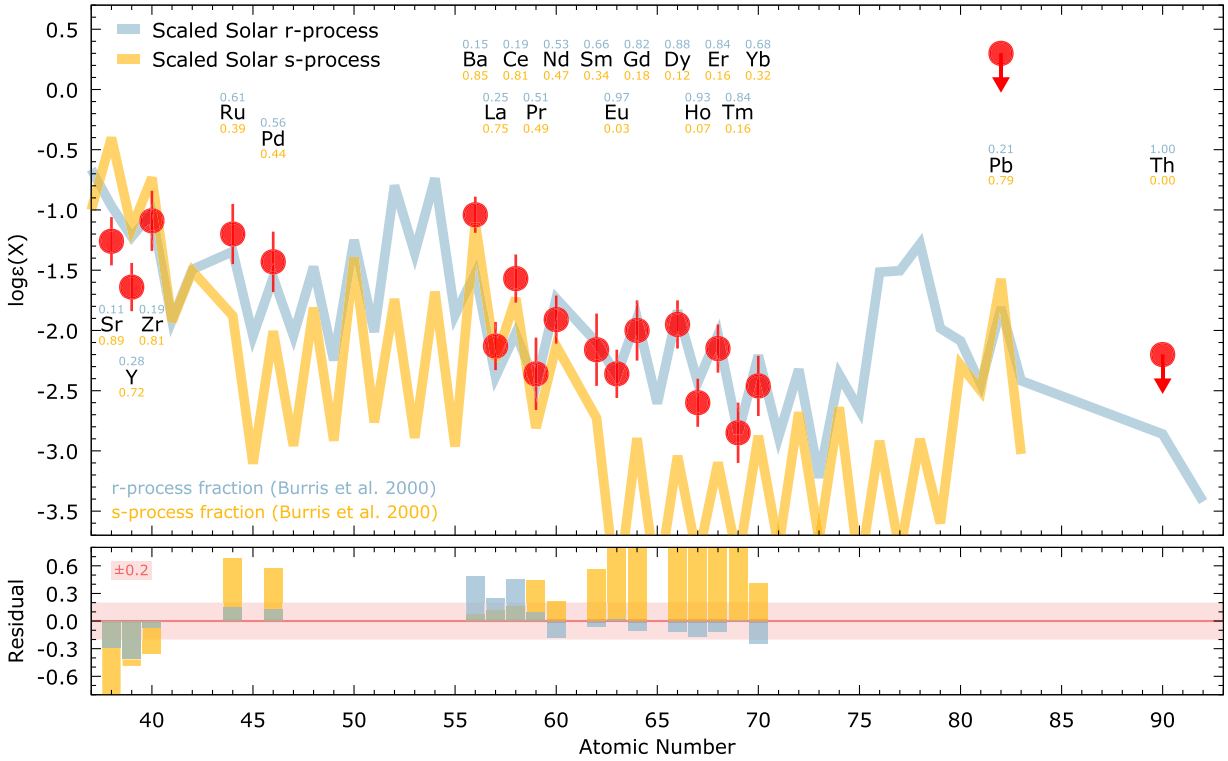

Figure 9. Upper panel: heavy-element chemical abundance pattern of RAVE J1830−4555, compared with the scaled solar system abundances. The *r*- and *s*-process contributions in the Sun are calculated based on the fractions given in Burris et al. (2000) and scaled to match the observed abundances of Eu and Ba, respectively. Lower panel: residuals between observations and the scaled solar system abundance patterns.

([La/Eu] = −0.35), yet the upper limit for the ratio of lead to europium exceeds the threshold, at [Pb/Eu] < +1.43, potentially making it consistent with the *s*-process expectation. However, even though the operation of the *s*-process at [Fe/H] < −3.5 is possible, the case of RAVE J1830−4555 would require both a high-mass AGB (donor) star and a binary system signature. Choplin et al. (2017) speculates that some CEMP-*s* stars, which appear to be single according to the radial-velocity monitoring program presented in Hansen et al. (2016a), could have been formed from the ejecta of low-metallicity *spinstars*. However, their [Fe/H] regime is somewhat higher than the value found for RAVE J1830−4555 and the models are also not able to reproduce high Pb abundances.

5.3.2. Comparison with Ejecta from a Neutron Star Merger Event

Given that the standard *s*- and *r*-process patterns are not a clear match to the chemical abundances of RAVE J1830−4555, we consider the possibility that a non-standard *r*-process could be responsible for the observed Ba, La, Ce, and Pb overproduction. For this exercise, we assume that RAVE J1830−4555 would have *measured* abundances of Pb and Th, set to be 0.4 and 0.5 dex lower than the estimated upper limits ($\log\epsilon\,(\mathrm{Pb}) = -0.10$ and $\log\epsilon\,(\mathrm{Th}) = -2.70$), respectively. These values would be consistent with measurements reported in the literature for stars in the same metallicity range: CS 30322-023 ([Fe/H] = −3.44 and $\log\epsilon\,(\mathrm{Pb}) = +0.10$; Masseron et al. 2006) and CS 30315-029 ([Fe/H] = −3.43 and $\log\epsilon\,(\mathrm{Th}) = -2.45$; Siqueira Mello et al. 2014). Figure 10 compares the chemical abundances of RAVE J1830−4555 (for $Z \geqslant 56$) with theoretical predictions for very fast ($v > 0.5c$) ejecta from a neutron star merger event. For the example calculations shown here, we take two tracers from the SFHO-M1.35 model of Bovard et al. (2017), which simulates the merger of two 1.35 $M_\odot$ neutron stars. This model considers binary neutron star systems on quasicircular orbits and initial configurations built from three different equations of state. The flow of ejected material is followed by tracer particles or measured on spherical surfaces at fixed distances from the center of the event (see Bovard et al. 2017, for further details). The nucleosynthesis calculations are from Wang et al. (2020), where details of the calculation appear and the outcome of the full model set is shown. Here we focus on example tracers 0032 and 2131, which have high speeds, $v = 0.529c$ and $v = 0.539c$, and distinct initial electron fractions, $Y_e = 0.112$ and $Y_e = 0.342$, respectively.

When neutron-rich material is ejected from an *r*-process event at very high speeds, the temperature and density evolve so quickly that a large neutron excess persists through the late stages of the *r*-process. In this scenario, neutron capture can continue throughout the decay to stability, shifting the second peak into the barium region and the third peak to the lead region. The resulting final elemental patterns are a good fit to RAVE J1830−4555 abundances for $Z \geqslant 56$, especially for Ba, La, and Ce. Though speculative, this type of fast *r*-process provides a consistent explanation for the unusual abundance features of RAVE J1830−4555. One possible way of testing the hypothesis of shifting the third peak to the lead region would be to compare upper limits for Os ($Z = 76$) or Ir ($Z = 77$) that are either at or lower than the scaled solar *r*-process pattern.

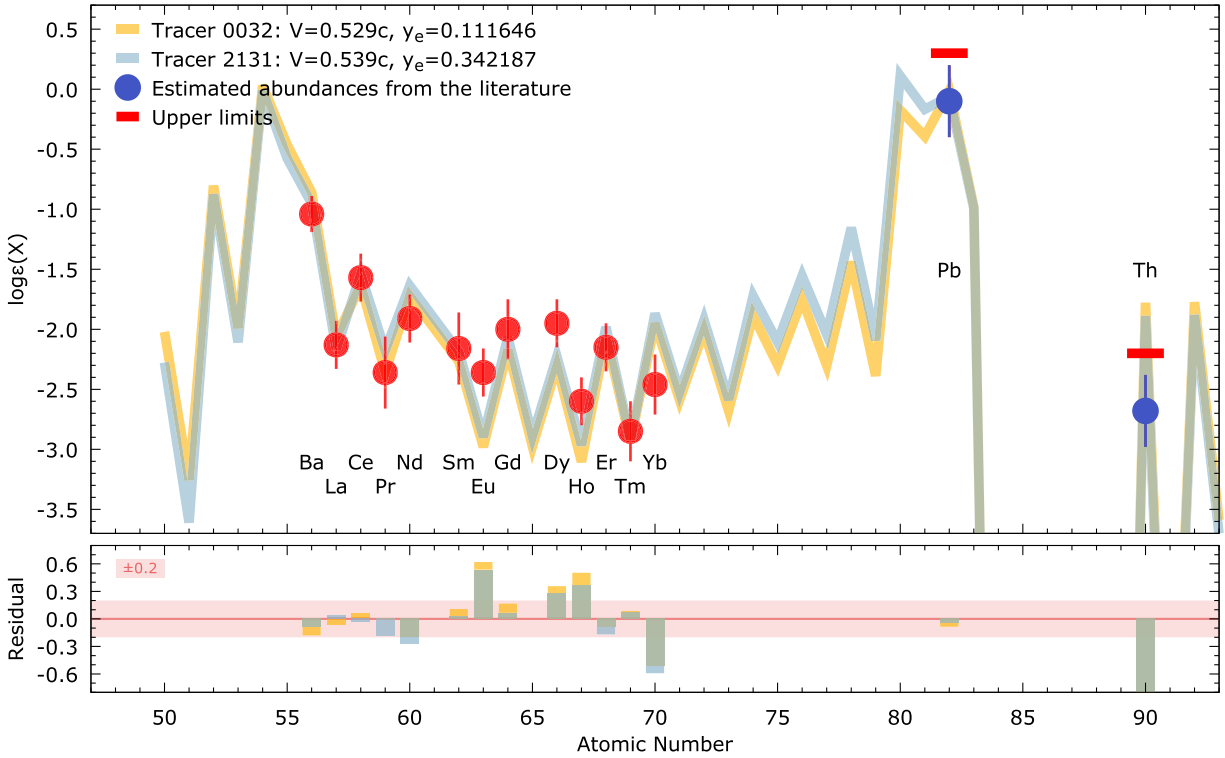

Figure 10. Upper panel: heavy-element chemical abundance pattern of RAVE J1830−4555 (see text for explanations of the choices for the Pb and Th values—upper limits also shown for reference), compared with the *r*-process nucleosynthesis yields for two very fast ($v > 0.5c$) example tracers 0032 and 2131 from a simulation of a neutron star merger (Bovard et al. 2017). The abundance pattern is scaled to match the observed abundance of Ce. Lower panel: residuals between observations and the scaled abundance patterns of fast *r*-process ejecta.

5.3.3. *Comparison with* r- *and* s-*processes in Massive Stars*

Non-rotating massive stars are known to experience a weak *s*-process, mainly during the core helium-burning phase (e.g., Langer et al. 1989; Prantzos et al. 1990; Raiteri et al. 1991). Rotational mixing can significantly boost the *s*-process in massive stars (Pignatari et al. 2008; Frischknecht et al. 2016; Choplin et al. 2018; Limongi & Chieffi 2018; Banerjee et al. 2019). Indeed, during the core helium-burning phase, rotation-induced mixing progressively transports ^{12}C and ^{16}O from the helium core to the hydrogen shell. It boosts the CNO cycle and produces extra ^{13}C and ^{14}N. These newly synthesized elements are engulfed by the convective helium core. Some ^{22}Ne is synthesized through the chain ^{14}N(α, γ)^{18}F(β^+)^{18}O(α, γ)^{22}Ne. Neutrons are then released through the ^{13}C(α, n) and ^{22}Ne(α, n) reactions. A massive star dying as a jet-like magnetorotational supernova or as a collapsar may also experience an *r*-process event (e.g., Winteler et al. 2012; Nishimura et al. 2015; Siegel et al. 2019).

We calculate the *s*-process patterns thanks to a one-zone nucleosynthesis code mimicking the core helium-burning phase of a rotating massive star. The code follows the central temperature and density of a complete 25 $M_\odot$ stellar model during core helium-burning. The initial chemical composition is taken from a low-metallicity stellar model at core helium-burning ignition. The initial abundances of elements heavier than Fe are set equal to zero. The initial Fe mass fraction is 2.03×10^{-7}, which corresponds to [Fe/H] $= -3.5$ (using the solar abundances of Asplund et al. 2009). During the nucleosynthesis calculation, ^{13}C and ^{14}N are injected at a constant rate in order to mimic the effect of rotational mixing during stellar evolution (see Choplin et al. 2016, for details about the injection method). We also consider an *r*-process contribution from a magnetorotational supernova model of Nishimura et al. (2015). We selected their B11β1.00 model, which has an initial magnetic field of 10^{11} G and a ratio of rotational energy to gravitational binding energy of 10^{-2} (see their Table 1).

The best fit when considering only an *s*-process (*r*-process) event is shown by the yellow (blue) line in Figure 11. The amount of added hydrogen is taken as a free parameter to minimize the χ^2 value (adding hydrogen has the effect of shifting the pattern down). The best fit when combining the two sets of yields is shown by the black line. In this case the dilution factor between the *s*- and *r*-process material is also set as a free parameter. If the Pb and Th abundances are set as measurements instead of upper limits, a reasonable agreement can also be found if considering a stronger *s*-process (Figure 12). The high Pb abundance can be reproduced if the injection rate of ^{13}C and ^{14}N is increased by a factor of 30 during the *s*-process calculation. This would correspond to a stronger rotation-induced mixing during stellar evolution.

Although we considered rotating massive stars as *s*-process sources in this exercise, an *s*-process originating from AGB stars cannot be excluded. If the *s*-process pattern comes from an AGB star, two astrophysical sources are required to explain the heavy-element abundance pattern of RAVE J1830−4555 (an AGB source and an *r*-process source). By contrast, if the *s*-process comes from a rotating massive star, just one source could be sufficient since a rotating massive star could produce both the *s*-process pattern during stellar evolution and the *r*-process pattern at the time of the supernova (e.g., during magnetorotational supernova or collapsar).

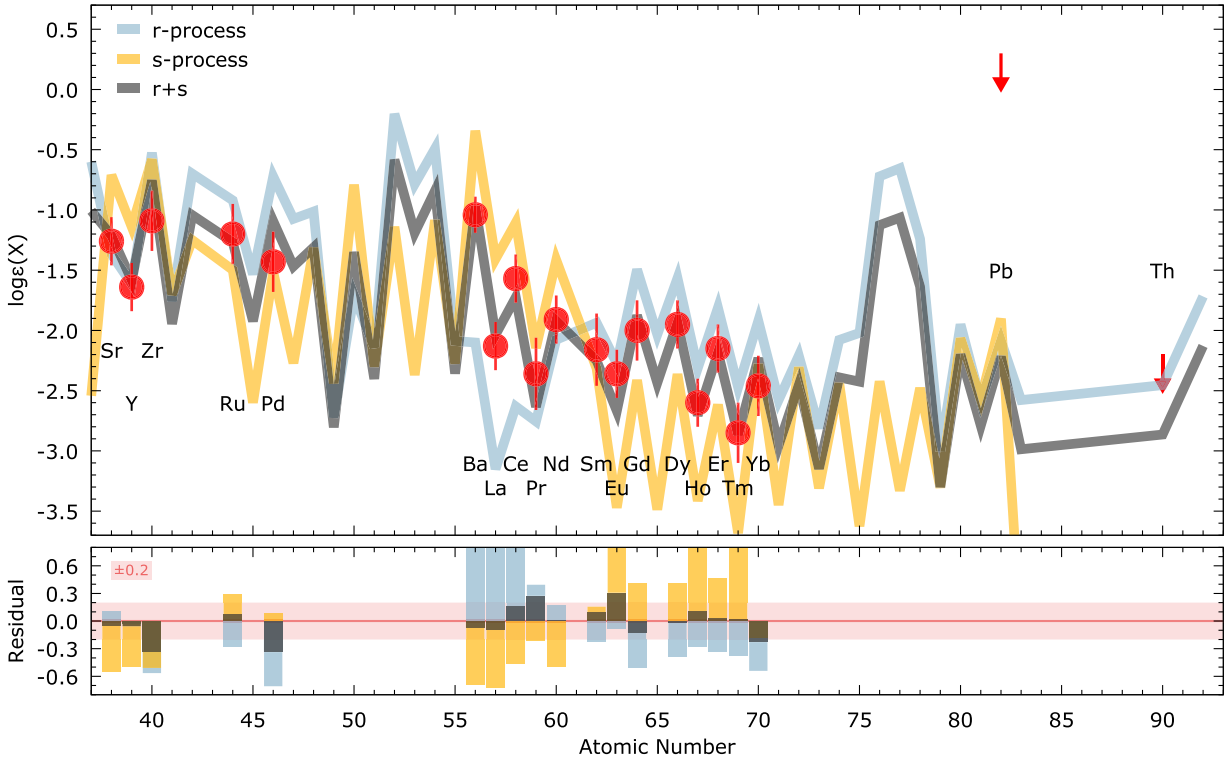

Figure 11. Best fits for trans-iron elements, if considering *s*-process only (yellow), *r*-process only (blue), and a combination of *s*- and *r*-processes (black, see text for details).

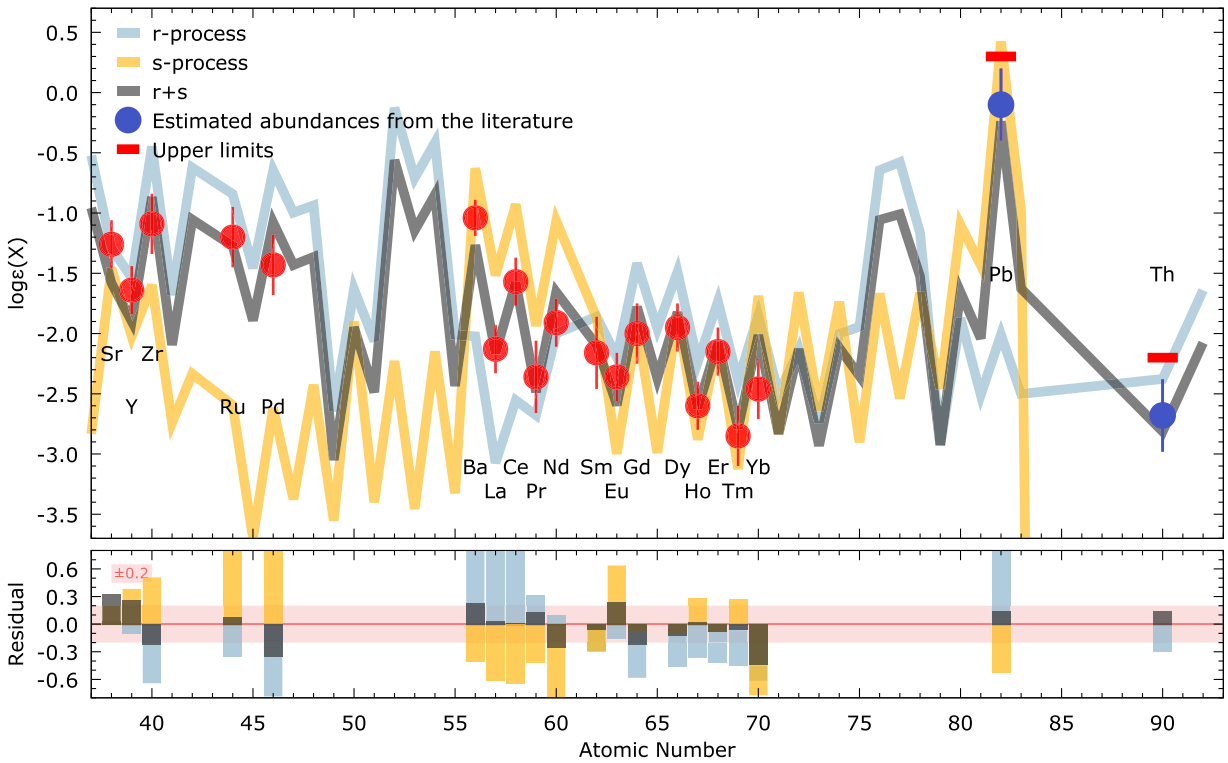

Figure 12. Same as Figure 11, but considering Pb and Th as measurements (see text for details). In this case, a stronger *s*-process is required to reproduce the Pb abundance, and the *r*-process pattern is the same as in Figure 11.

In this scenario, the massive star cannot be a Population III star, since the *s*-process is a secondary process that requires some heavy seeds (e.g., Fe) during stellar evolution. Without these heavy seeds (i.e., in the case of a Population III star), the *s*-process would be too weak (or even non-existent) and the *s*-process abundances (e.g., Ba) of RAVE J1830−4555 could not be reproduced. Thus, a possible scenario would be that one (or more) Population III massive stars first exploded (similar to

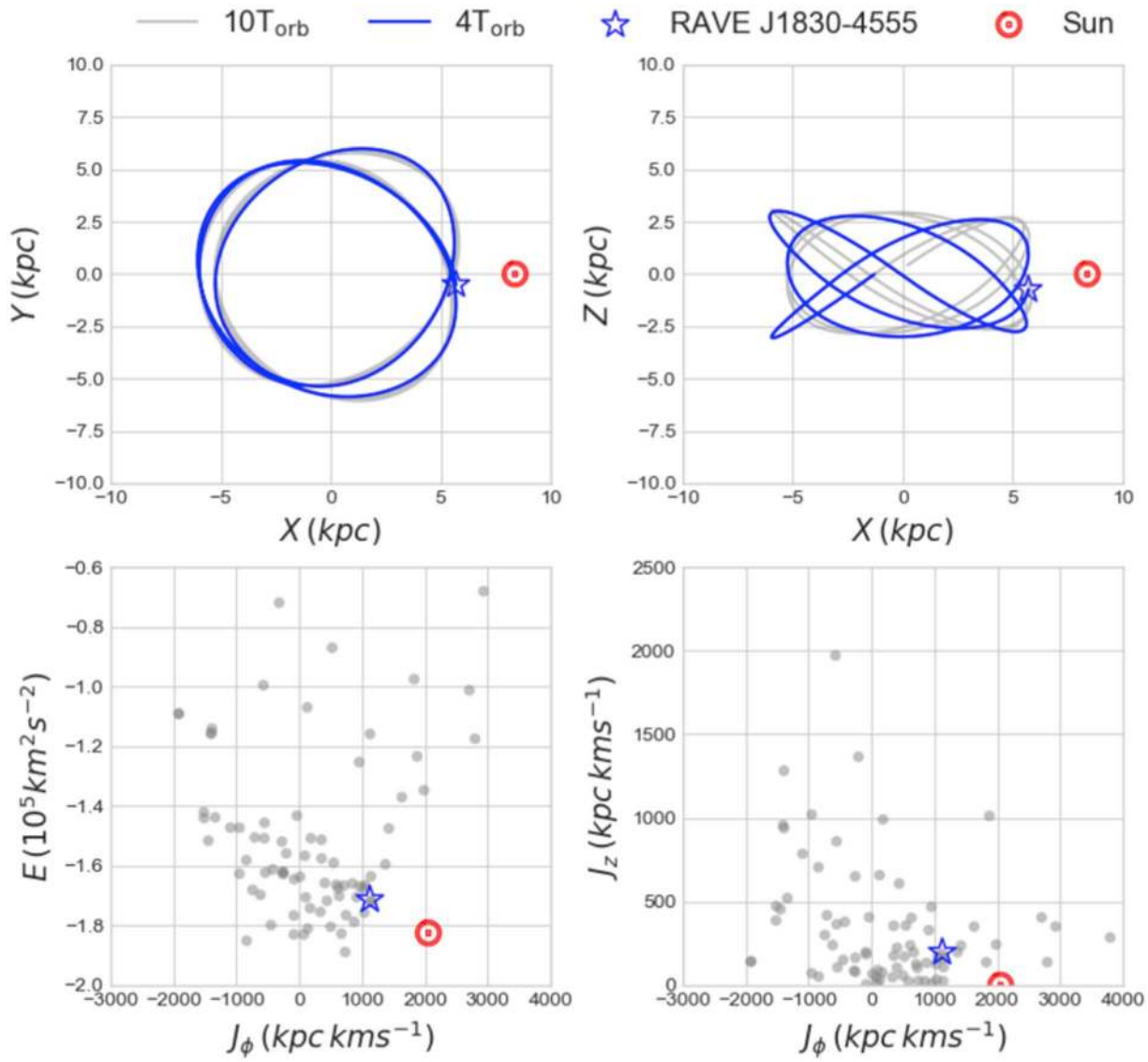

Figure 13. Upper panels: integrated orbit for RAVE J1830−4555 (current position marked as a blue star) over its last 10 periods (gray line—1.0 Gyr look-back time) and four periods (blue line—0.4 Gyr look-back time) in the *xy* and *xz* planes. Lower panels: behavior of RAVE J1830−4555 in two different planes of orbital energy vs. action, compared with data from Roederer et al. (2018a) for *r*-process enhanced stars. The current position of the Sun in all panels is marked with a red circle.

the progenitor suggested in Section 5.2) and injected some Fe into the interstellar medium (up to [Fe/H] ~ -3.5), and then a second-generation rotating massive star formed, exploded as a magnetorotational supernova or collapsar, and enriched the interstellar medium with a mixture of *s*- and *r*-process elements. Then RAVE J1830−4555 formed as a third-generation star.

5.4. Orbital Properties

In this section, we investigate the orbital properties of RAVE J1830−4555, using the measurements of proper motion from Gaia DR2 (Lindegren et al. 2018). We take the distance determined from the `StarHorse` code (Anders et al. 2019), which uses a Bayesian method combining the parallaxes and optical photometry to derive the stellar parameters and distances, and sets the parallax zero-point offset to be +0.05 mas for bright sources. The radial velocity is taken from the Magellan spectrum. All of the kinematic parameters used in these calculations are listed in Table 1. The values of solar motion used are (U, V, W) = (11.10, 12.24, 7.25) km s^{-1} (Schönrich et al. 2019), and the motion of the LSR is $v_{\rm LSR}$ = 232.8 km s^{-1} (McMillan 2011). We then calculate the orbital energy of RAVE J1830−4555 and trace its orbit in the gravitational potential of McMillan (2017) using AGAMA (Vasiliev 2019). In addition, we generate 10^4 realizations of the same set of parameters by sampling the distances assuming a Gaussian distribution according to its 16th and 84th percentile values, as well as the proper motions by taking into account their observational errors and covariance matrix.

The integrated orbit of RAVE J1830−4555 over the last 10 periods (1.0 Gyr look-back time) is indicated as a gray line in the upper panels of Figure 13. The orbit over the last four periods (0.4 Gyr look-back time) is highlighted in blue. This orbit integration clearly shows that RAVE J1830−4555 possesses a very circular motion in the Galactic plane and a small vertical motion in the Z direction, confined within $z_{\rm max} = 3.1^{+0.5}_{-0.4}$ kpc. This is consistent with its low eccentricity $e = 0.125^{+0.12}_{-0.11}$, and may be associated with the MWTD. This

can be also be inferred from inspection of the (E, J_ϕ) and (J_z, J_ϕ) planes shown in the lower panels of Figure 13, where the gray circles represent the 89 *r*-process enhanced stars from Roederer et al. (2018a). Compared to the solar values, RAVE J1830−4555 has a lower orbital energy, which is consistent with its smaller pericentric and apocentric distances ($r_{\rm peri} = 5.26^{+0.15}_{-0.16}$ kpc, $r_{\rm apo} = 6.77^{+0.35}_{-0.35}$ kpc). RAVE J1830−4555 also has a non-negligible action in the Z direction with $J_z = 202.5^{+65.1}_{-61.9}$ kpc km s^{-1}.

In summary, RAVE J1830−4555 has typical MWTD dynamics. It was very likely born in situ and its orbit was heated during early merger events. Alternatively, RAVE J1830−4555 could have come from accreted systems with very prograde orbits. Sestito et al. (2020) argues that a star such as RAVE J1830−4555 could be the by-product, at early times, of the assembly of the proto-Galaxy, minor mergers, or in-situ formation.

6. Conclusions

We have presented the first high-resolution spectroscopic study of the extremely metal-poor, CNO-enhanced star RAVE J1830−4555. This star shows an intriguing chemical abundance pattern, combining a light-element abundance pattern that resembles that of a "mono-enriched" star with a heavy-element pattern matching either that from the fast ejecta from a neutron star merger event or that from a rotating massive star experiencing an *r*-process event during its explosion. Measurements of lead and thorium abundances in stars similar to RAVE J1830−4555 would help to distinguish between these (and other) possible formation scenarios. The lack of radial-velocity variations suggests that RAVE J1830−4555 is not in a binary system, ruling out the possibility of chemical enrichment via mass transfer from an evolved companion. Analysis of the orbital parameters derived from Gaia DR2 data places RAVE J1830−4555 in the MWTD population of the Milky Way, presenting interesting constraints on the population of its progenitor(s). At [Fe/H] < -3.5, this peculiar third-generation star could have been formed in situ or during the early stages of the assembly of the Milky Way.

The authors thank Fiorenzo Vincenzo for providing feedback on the first version of this manuscript. The authors acknowledge partial support for this work from the National Science Foundation (NSF) under grant No. PHY-1430152 (Physics Frontier Center/JINA Center for the Evolution of the Elements). R.M.S. acknowledges support from CNPq (Project 436696/2018-5) and CAPES/PROAP-IF. R.S. and X.W. acknowledge support from the Department of Energy Contract No. DE-FG02-95-ER40934 and National Science Foundation Contract No. PHY-1630782 Focused Research Hub in Theoretical Physics: Network for Neutrinos, Nuclear Astrophysics, and Symmetries (N3AS). I.U.R. acknowledges financial support from grants AST 16-13536 and AST-1815403, awarded by the NSF. A.C. acknowledges funding from the Swiss National Science Foundation under grant P2GEP2_184492. A.P.J. is supported by NASA through Hubble Fellowship grant HST-HF2-51393.001 awarded by the Space Telescope Science Institute, which is operated by the Association of Universities for Research in Astronomy, Inc., for NASA, under contract NAS5-26555. A.F. is supported by NSF CAREER grant AST-1255160. This research has made use of NASA's Astrophysics Data System Bibliographic Services; the arXiv preprint server operated by Cornell University; the SIMBAD database hosted by the Strasbourg Astronomical Data Center; the IRAF software packages distributed by the National Optical Astronomy Observatories, which are operated by AURA, under cooperative agreement with the NSF; the SAGA Database (Stellar Abundances for Galactic Archeology; Suda et al. 2008); the JINAbase chemical abundance database (Abohalima & Frebel 2018); and the online Q&A platform `stackoverflow` (http://stackoverflow.com/). This research was made possible through the use of the AAVSO Photometric All-Sky Survey (APASS), funded by the Robert Martin Ayers Sciences Fund. This publication makes use of data products from the Two Micron All Sky Survey, which is a joint project of the University of Massachusetts and the Infrared Processing and Analysis Center/California Institute of Technology, funded by the National Aeronautics and Space Administration and the National Science Foundation. This work has made use of data from the European Space Agency (ESA) mission Gaia (https://www.cosmos.esa.int/gaia), processed by the Gaia Data Processing and Analysis Consortium (DPAC, https://www.cosmos.esa.int/wdpac/consortium). Funding for the DPAC has been provided by national institutions, in particular the institutions participating in the Gaia Multilateral Agreement.

Software: `awk` (Aho et al. 1987), `gnuplot` (Williams & Kelley 2015), `IRAF` (Tody 1986, 1993), `matplotlib` (Hunter 2007), `n-SSPP` (Beers et al. 2014), `numpy` (Oliphant 2006), `pandas` (McKinney 2010), `R-project` (R Core Team 2015), `sed` (Mcmahon 1979).

ORCID iDs

Vinicius M. Placco https://orcid.org/0000-0003-4479-1265
Rafael M. Santucci https://orcid.org/0000-0002-7529-1442
Zhen Yuan https://orcid.org/0000-0002-8129-5415
Mohammad K. Mardini https://orcid.org/0000-0001-9178-3992
Erika M. Holmbeck https://orcid.org/0000-0002-5463-6800
Xilu Wang https://orcid.org/0000-0002-5901-9879
Rebecca Surman https://orcid.org/0000-0002-4729-8823
Terese T. Hansen https://orcid.org/0000-0001-6154-8983
Ian U. Roederer https://orcid.org/0000-0001-5107-8930
Timothy C. Beers https://orcid.org/0000-0003-4573-6233
Arthur Choplin https://orcid.org/0000-0001-6159-8470
Alexander P. Ji https://orcid.org/0000-0002-4863-8842
Rana Ezzeddine https://orcid.org/0000-0002-8504-8470
Anna Frebel https://orcid.org/0000-0002-2139-7145
Charli M. Sakari https://orcid.org/0000-0002-5095-4000
Devin D. Whitten https://orcid.org/0000-0002-9594-6143
Joseph Zepeda https://orcid.org/0000-0003-0998-2744

References

Abbott, B. P., Abbott, R., Abbott, T. D., et al. 2017, ApJL, 848, L12
Abohalima, A., & Frebel, A. 2018, ApJS, 238, 36
Aguado, D. S., Allende Prieto, C., González Hernández, J. I., & Rebolo, R. 2018, ApJL, 854, L34
Aho, A. V., Kernighan, B. W., & Weinberger, P. J. 1987, The AWK Programming Language (Boston, MA: Addison-Wesley Longman)
Anders, F., Khalatyan, A., Chiappini, C., et al. 2019, A&A, 628, A94
Aoki, W., Beers, T. C., Christlieb, N., et al. 2007, ApJ, 655, 492
Arnett, D. 1996, Supernovae and Nucleosynthesis: An Investigation of the History of Matter from the Big Bang to the Present (Princeton, NJ: Princeton Univ. Press)
Asplund, M., Grevesse, N., Sauval, A. J., & Scott, P. 2009, ARA&A, 47, 481

Bailer-Jones, C. A. L., Rybizki, J., Fouesneau, M., Mantelet, G., & Andrae, R. 2018, AJ, 156, 58
Banerjee, P., Heger, A., & Qian, Y.-Z. 2019, ApJ, 887, 187
Beers, T. C., & Christlieb, N. 2005, ARA&A, 43, 531
Beers, T. C., Norris, J. E., Placco, V. M., et al. 2014, ApJ, 794, 58
Beers, T. C., Placco, V. M., Carollo, D., et al. 2017, ApJ, 835, 81
Bernstein, R., Shectman, S. A., Gunnels, S. M., Mochnacki, S., & Athey, A. E. 2003, Proc. SPIE, 4841, 1694
Bovard, L., Martin, D., Guercilena, F., et al. 2017, PhRvD, 96, 124005
Bromm, V., & Larson, R. B. 2004, ARA&A, 42, 79
Bromm, V., Yoshida, N., Hernquist, L., & McKee, C. F. 2009, Natur, 459, 49
Burbidge, E. M., Burbidge, G. R., Fowler, W. A., & Hoyle, F. 1957, RvMP, 29, 547
Burris, D. L., Pilachowski, C. A., Armandroff, T. E., et al. 2000, ApJ, 544, 302
Buzzoni, B., Delabre, B., Dekker, H., et al. 1984, Msngr, 38, 9
Caffau, E., Bonifacio, P., François, P., et al. 2011, Natur, 477, 67
Caffau, E., Bonifacio, P., Spite, M., et al. 2016, A&A, 595, L6
Cain, M., Frebel, A., Gull, M., et al. 2018, ApJ, 864, 43
Cameron, A. G. W. 1957, PASP, 69, 201
Castelli, F., & Kurucz, R. L. 2003, in IAU Symp. 210, Modelling of Stellar Atmospheres, Poster Contributions, ed. N. Piskunov, W. W. Weiss, & D. F. Gray (San Francisco, CA: ASP), A20
Cescutti, G., & Chiappini, C. 2014, A&A, 565, A51
Cescutti, G., Chiappini, C., Hirschi, R., Meynet, G., & Frischknecht, U. 2013, A&A, 553, A51
Cescutti, G., Romano, D., Matteucci, F., Chiappini, C., & Hirschi, R. 2015, A&A, 577, A139
Chiappini, C. 2013, AN, 334, 595
Choplin, A., Hirschi, R., Meynet, G., & Ekström, S. 2017, A&A, 607, L3
Choplin, A., Hirschi, R., Meynet, G., et al. 2018, A&A, 618, A133
Choplin, A., Maeder, A., Meynet, G., & Chiappini, C. 2016, A&A, 593, A36
Christlieb, N., Bessell, M. S., Beers, T. C., et al. 2002, Natur, 419, 904
Cohen, J. G., Christlieb, N., McWilliam, A., et al. 2008, ApJ, 672, 320
Cohen, J. G., Christlieb, N., Thompson, I., et al. 2013, ApJ, 778, 56
Cooke, R., & Madau, P. 2014, ApJ, 791, 116
Cooke, R., Pettini, M., Steidel, C. C., Rudie, G. C., & Nissen, P. E. 2011, MNRAS, 417, 1534
Côté, B., Eichler, M., Arcones, A., et al. 2019, ApJ, 875, 106
Cseh, B., Lugaro, M., D'Orazi, V., et al. 2018, A&A, 620, A146
Drout, M. R., Piro, A. L., Shappee, B. J., et al. 2017, Sci, 358, 1570
Ezzeddine, R., Frebel, A., Roederer, I. U., et al. 2019, ApJ, 876, 97
Ezzeddine, R., Rasmussen, K., Frebel, A., et al. 2020, ApJ, in press
Frebel, A. 2018, ARNPS, 68, 237
Frebel, A., Casey, A. R., Jacobson, H. R., & Yu, Q. 2013, ApJ, 769, 57
Frebel, A., Chiti, A., Ji, A. P., Jacobson, H. R., & Placco, V. M. 2015, ApJL, 810, L27
Frebel, A., Christlieb, N., Norris, J. E., et al. 2006, ApJ, 652, 1585
Frebel, A., & Norris, J. E. 2015, ARA&A, 53, 631
Frischknecht, U., Hirschi, R., Pignatari, M., et al. 2016, MNRAS, 456, 1803
Gaia Collaboration, Brown, A. G. A., Vallenari, A., et al. 2018, A&A, 616, A1
Grichener, A., & Soker, N. 2019, ApJ, 878, 24
Gull, M., Frebel, A., Cain, M. G., et al. 2018, ApJ, 862, 174
Hampel, M., Stancliffe, R. J., Lugaro, M., & Meyer, B. S. 2016, ApJ, 831, 171
Hansen, C. J., Hansen, T. T., Koch, A., et al. 2019, A&A, 623, A128
Hansen, T., Andersen, J., Nordström, B., Buchhave, L. A., & Beers, T. C. 2011, ApJL, 743, L1
Hansen, T., Hansen, C. J., Christlieb, N., et al. 2014, ApJ, 787, 162
Hansen, T. T., Andersen, J., Nordström, B., et al. 2015, A&A, 583, A49
Hansen, T. T., Andersen, J., Nordström, B., et al. 2016a, A&A, 588, A3
Hansen, T. T., Andersen, J., Nordström, B., et al. 2016b, A&A, 586, A160
Hansen, T. T., Holmbeck, E. M., Beers, T. C., et al. 2018, ApJ, 858, 92
Hansen, T. T., Simon, J. D., Marshall, J. L., et al. 2017, ApJ, 838, 44
Hartwig, T., Yoshida, N., Magg, M., et al. 2018, MNRAS, 478, 1795
Haynes, C. J., & Kobayashi, C. 2019, MNRAS, 483, 5123
Heger, A., & Woosley, S. E. 2010, ApJ, 724, 341
Henden, A., & Munari, U. 2014, CoSka, 43, 518
Herwig, F. 2005, ARA&A, 43, 435
Holmbeck, E., Hansen, T. T., Beers, T. C., Placco, V. M., & Frebel, A. L. 2020, ApJ, in press
Holmbeck, E. M., Beers, T. C., Roederer, I. U., et al. 2018, ApJL, 859, L24
Holmbeck, E. M., Sprouse, T. M., Mumpower, M. R., et al. 2019, ApJ, 870, 23
Hoyle, F. 1954, ApJS, 1, 121
Hunter, J. D. 2007, CSE, 9, 90
Ishimaru, Y., Wanajo, S., & Prantzos, N. 2015, ApJL, 804, L35
Ito, H., Aoki, W., Beers, T. C., et al. 2013, ApJ, 773, 33
Jacobson, H. R., Keller, S., Frebel, A., et al. 2015, ApJ, 807, 171
Ji, A. P., Drout, M. R., & Hansen, T. T. 2019, ApJ, 882, 40
Ji, A. P., Frebel, A., Chiti, A., & Simon, J. D. 2016, Natur, 531, 610
Keller, S. C., Bessell, M. S., Frebel, A., et al. 2014, Natur, 506, 463
Kelson, D. D. 2003, PASP, 115, 688
Kunder, A., Kordopatis, G., Steinmetz, M., et al. 2017, AJ, 153, 75
Langer, N., Arcoragi, J.-P., & Arnould, M. 1989, A&A, 210, 187
Lasker, B. M., Sturch, C. R., McLean, B. J., et al. 1990, AJ, 99, 2019
Lee, Y. S., Beers, T. C., Masseron, T., et al. 2013, AJ, 146, 132
Lee, Y. S., Beers, T. C., Sivarani, T., et al. 2008a, AJ, 136, 2022
Lee, Y. S., Beers, T. C., Sivarani, T., et al. 2008b, AJ, 136, 2050
Limongi, M., & Chieffi, A. 2018, ApJS, 237, 13
Lindegren, L., Hernández, J., Bombrun, A., et al. 2018, A&A, 616, A2
Longeard, N., Martin, N., Starkenburg, E., et al. 2018, MNRAS, 480, 2609
Mardini, M. K., Li, H., Placco, V. M., et al. 2019a, ApJ, 875, 89
Mardini, M. K., Placco, V. M., Taani, A., Li, H., & Zhao, G. 2019b, ApJ, 882, 27
Marshall, J. L., Hansen, T., Simon, J. D., et al. 2019, ApJ, 882, 177
Masseron, T., van Eck, S., Famaey, B., et al. 2006, A&A, 455, 1059
Matteucci, F., Romano, D., Arcones, A., Korobkin, O., & Rosswog, S. 2014, MNRAS, 438, 2177
McKinney, W. 2010, in Proc. of the 9th Python in Science Conference (SciPy 2010) (Austin, TX), ed. S. van der Walt & J. Millman, 56, https://conference.scipy.org/proceedings/scipy2010/mckinney.html
Mcmahon, L. E. 1979, UNIX Programmery Manual—7th Edition, Vol. 2 (Murray Hill, NJ: Bell Telephone Laboratories)
McMillan, P. J. 2011, MNRAS, 414, 2446
McMillan, P. J. 2017, MNRAS, 465, 76
Meléndez, J., Placco, V. M., Tucci-Maia, M., et al. 2016, A&A, 585, L5
Merrill, P. W. 1952, ApJ, 116, 21
Meynet, G., Hirschi, R., Ekstrom, S., et al. 2010, A&A, 521, A30
Nagasawa, D. Q., Marshall, J. L., Li, T. S., et al. 2018, ApJ, 852, 99
Nishimura, N., Takiwaki, T., & Thielemann, F.-K. 2015, ApJ, 810, 109
Nomoto, K., Kobayashi, C., & Tominaga, N. 2013, ARA&A, 51, 457
Nomoto, K., Tominaga, N., Umeda, H., Kobayashi, C., & Maeda, K. 2006, NuPhA, 777, 424
Norris, J. E., Christlieb, N., Korn, A. J., et al. 2007, ApJ, 670, 774
Oliphant, T. E. 2006, A Guide to NumPy, Vol. 1 (USA: Trelgol Publishing), http://www.numpy.org/
Pignatari, M., Gallino, R., Meynet, G., et al. 2008, ApJL, 687, L95
Placco, V. M., Beers, T. C., Ivans, I. I., et al. 2015, ApJ, 812, 109
Placco, V. M., Beers, T. C., Reggiani, H., & Meléndez, J. 2016a, ApJL, 829, L24
Placco, V. M., Beers, T. C., Roederer, I. U., et al. 2014a, ApJ, 790, 34
Placco, V. M., Beers, T. C., Santucci, R. M., et al. 2018, AJ, 155, 256
Placco, V. M., Frebel, A., Beers, T. C., et al. 2013, ApJ, 770, 104
Placco, V. M., Frebel, A., Beers, T. C., et al. 2014b, ApJ, 781, 40
Placco, V. M., Frebel, A., Beers, T. C., et al. 2016b, ApJ, 833, 21
Placco, V. M., Frebel, A., Beers, T. C., & Stancliffe, R. J. 2014c, ApJ, 797, 21
Placco, V. M., Santucci, R. M., Beers, T. C., et al. 2019, ApJ, 870, 122
Prantzos, N., Abia, C., Cristallo, S., Limongi, M., & Chieffi, A. 2020, MNRAS, 491, 1832
Prantzos, N., Hashimoto, M., & Nomoto, K. 1990, A&A, 234, 211
R Core Team 2015, R: A Language and Environment for Statistical Computing (Vienna, Austria: The R Foundation for Statistical Computing), https://www.R-project.org
Raiteri, C. M., Busso, M., Gallino, R., Picchio, G., & Pulone, L. 1991, ApJ, 367, 228
Roederer, I. U. 2017, ApJ, 835, 23
Roederer, I. U., Cowan, J. J., Karakas, A. I., et al. 2010, ApJ, 724, 975
Roederer, I. U., Hattori, K., & Valluri, M. 2018a, AJ, 156, 179
Roederer, I. U., Lawler, J. E., Sobeck, J. S., et al. 2012, ApJS, 203, 27
Roederer, I. U., Placco, V. M., & Beers, T. C. 2016, ApJL, 824, L19
Roederer, I. U., Preston, G. W., Thompson, I. B., Shectman, S. A., & Sneden, C. 2014a, ApJ, 784, 158
Roederer, I. U., Preston, G. W., Thompson, I. B., et al. 2014b, AJ, 147, 136
Roederer, I. U., Sakari, C. M., Placco, V. M., et al. 2018b, ApJ, 865, 129
Sakari, C. M., Placco, V. M., Farrell, E. M., et al. 2018a, ApJ, 868, 110
Sakari, C. M., Placco, V. M., Hansen, T., et al. 2018b, ApJL, 854, L20
Salvadori, S., Skúladóttir, Á., & Tolstoy, E. 2015, MNRAS, 454, 1320
Schlafly, E. F., & Finkbeiner, D. P. 2011, ApJ, 737, 103
Schönrich, R., McMillan, P., & Eyer, L. 2019, MNRAS, 487, 3568
Sestito, F., Martin, N. F., Starkenburg, E., et al. 2020, MNRAS Letters, 497, L7
Shappee, B. J., Simon, J. D., Drout, M. R., et al. 2017, Sci, 358, 1574
Shen, S., Cooke, R. J., Ramirez-Ruiz, E., et al. 2015, ApJ, 807, 115
Siegel, D. M., Barnes, J., & Metzger, B. D. 2019, Natur, 569, 241
Siqueira Mello, C., Hill, V., Barbuy, B., et al. 2014, A&A, 565, A93

Skrutskie, M. F., Cutri, R. M., Stiening, R., et al. 2006, AJ, 131, 1163
Sneden, C., Cowan, J. J., & Gallino, R. 2008, ARA&A, 46, 241
Sneden, C. A. 1973, PhD thesis, The Univ. of Texas at Austin
Starkenburg, E., Aguado, D. S., Bonifacio, P., et al. 2018, MNRAS, 481, 3838
Starkenburg, E., Shetrone, M. D., McConnachie, A. W., & Venn, K. A. 2014, MNRAS, 441, 1217
Steinmetz, M., Zwitter, T., Siebert, A., et al. 2006, AJ, 132, 1645
Suda, T., Katsuta, Y., Yamada, S., et al. 2008, PASJ, 60, 1159
Tody, D. 1986, Proc. SPIE, 627, 733
Tody, D. 1993, in ASP Conf. Ser. 52, Astronomical Data Analysis Software and Systems II, ed. R. J. Hanisch, R. J. V. Brissenden, & J. Barnes (San Francisco, CA: ASP), 173
Tominaga, N., Iwamoto, N., & Nomoto, K. 2014, ApJ, 785, 98
Umeda, H., & Nomoto, K. 2005, ApJ, 619, 427
van de Voort, F., Quataert, E., Hopkins, P. F., Kereš, D., & Faucher-Giguère, C.-A. 2015, MNRAS, 447, 140
Vasiliev, E. 2019, MNRAS, 482, 1525
Vincenzo, F., Matteucci, F., Recchi, S., et al. 2015, MNRAS, 449, 1327
Wanajo, S., Itoh, N., Ishimaru, Y., Nozawa, S., & Beers, T. C. 2002, ApJ, 577, 853
Wang, X., Fields, B. D., Mumpower, M., et al. 2020, ApJ, 893, 92
Wehmeyer, B., Pignatari, M., & Thielemann, F.-K. 2015, MNRAS, 452, 1970
Welsh, L., Cooke, R., Fumagalli, M., & Pettini, M. 2020, MNRAS, 494, 1411
Williams, T., & Kelley, C. 2015, Gnuplot 5.0: An Interactive Plotting Program, http://www.gnuplot.info/
Winteler, C., Käppeli, R., Perego, A., et al. 2012, ApJL, 750, L22
Yoon, J., Beers, T. C., Placco, V. M., et al. 2016, ApJ, 833, 20
Yoon, J., Whitten, D. D., Beers, T. C., Lee, Y. S., & Placco, V. M. 2020, ApJ, 894, 7